FACILITY FORM 602

N70-36439 (ACCESSION NUMBER)
90 (PAGES)
CR-112401 (NASA CR OR TMX OR AD NUMBER)

N70-36446 (THRU)
1 (CODE)
07 (CATEGORY)

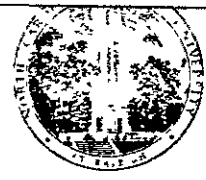

DEPARTMENT OF ELECTRICAL ENGINEERING

NORTH CAROLINA STATE UNIVERSITY

RALEIGH, NORTH CAROLINA

Reproduced by
NATIONAL TECHNICAL
INFORMATION SERVICE
Springfield, Va. 22151

PROGRESS REPORT
Grant NGR-34-002-047
June 15, 1970

NGL-

"STUDY OF
RECTANGULAR-GUIDE-LIKE STRUCTURES FOR
MILLIMETER WAVE TRANSMISSION"

to
The National Aeronautics and Space
Administration, Washington, D. C.

North Carolina State University
Raleigh, North Carolina

Submitted: F. J. Tischer

Dr. Frederick J. Tischer, Professor
Principal Investigator

PERSONNEL

Dr. Frederick J. Tischer, Principal Investigator

Mr. Lyles Adair, Graduate Student

Mr. K. K. Agarwal, Graduate Student

Mr. F. Jalali, Graduate Student

Mr. J. R. Potukuchi, Graduate Student

Mr. R. A. Kraft, Senior Undergraduate

Mr. M. D. Summerlin, Senior Undergraduate

TABLE OF CONTENTS

INTRODUCTION

This progress report presents results of research carried out under Grant NGL-34-002-047 during the period February 1 to May 31, 1970.

As a part of the efforts to use standardized symbols and notations in research under the grant, a list of notations related to wire grids is presented.

The report contains next a paper which appeared in the Transactions of the IEEE on Microwave Theory and Techniques in the January issue of 1970, and which deals with the H-guide with laminated dielectric. Lamination is one of the approaches to reduce the dielectric losses in the H-guide which contribute a major part of the attenuation of this guide. The study shows that a reduction of the loss tangent by a factor of about 10 can be achieved by this approach. The improvement can be obtained by using thin strips of low-loss material with high permittivity separated by layers of air or by layers of a foamed low-loss dielectric.

In an effort to reduce the wall losses in the waveguides under investigation, such as H-guides, fence guides, and reflector guides by proper treatment of the conductor surfaces, the effects of the surface roughness and surface structure on the attenuation are being investigated. Optical methods are used to measure appropriate parameters for the surface roughness. Various degrees of surface roughness are obtained by polishing the surfaces on papers of various grain sizes. Once calibrated, the optical setup permits simple but reliable measurement of the

surface roughness. The waveguides under investigation, in turn, permit accurate determination of the effects of surface roughness on the Q-value and on the surface resistance of the conducting surfaces. The measurements are expected to permit determination of optimum characteristics obtained by proper surface treatment.

A detailed study of the error sources of Q-value measurements was carried out which indicated the possibility of obtaining improvements by refining the measurement procedures and by eliminating frequency jitter resulting from vibrations entering the microwave oscillator used for the frequency measurement. A modulation oscillator for the X-band source was then added to the measurement setup which permitted simultaneous determination of the half-power frequencies. By the use of water cooling and vibration-free support of the X-band circuitry, frequency jitter of the X-band source was reduced considerably. As a consequence of these measures, the measurement error was reduced to about $\pm 0.2\%$. The changed procedures and the improved setup are described in part 4 of the report.

Discrepancies were observed at the comparison of measured and computed values of the attenuation of the fence guide. This made a review of the relationships used for the computation of the characteristics of wire grids necessary. It was found that the relationships derived and described in the literature are no longer valid for dense wire grids as used in the fence guide. New relationships were derived for the surface impedance which adequately describe the properties of wire grids with dimensions useful for the

fence guide. Equations for lossless and lossy wires were found. Derivations and the relationships are described in part 5 of this report.

Part 6 presents the results of measurements of the characteristics of the fence guide carried out on a prototype section of guide with a length of 175 mm. Two such sections with different spacings of the wires were fabricated and one of them investigated during the report period. Prior to the measurements, the measurement setup and the field probes were tested and improved to give increased accuracy and improved reproducibility. Longitudinal and transverse field distributions were then measured and the results evaluated. The results are presented in part 6 of the report. Reduction of the diameter of the compensated probe gave considerably improved results in comparison with those obtained in previous measurements. The measurements continue on the second section of fence guide with increased wire spacing.

An experimental study was carried out on a shorted section of open reflector guide previously investigated theoretically, (Progress Reports of June 15 and October 15, 1969). The shorted section represents a resonator whose Q-value and internal field distribution were measured. It was found that improved resonance conditions and improved Q-values (as high as 30,000) can be obtained by reducing the spacing of the reflector surfaces. To study the effect of a variation of the distance on the Q-value and the field distribution, one of the reflector surfaces was made movable. This permits determination of the characteristics of the resonator under nonfocal conditions. Preliminary results

of the measurements are presented in part 7 of the report.

As a part of the study of dielectric loading of H-guide and fence guides, the electromagnetic field-matching method has been studied. It was applied for finding the characteristics of a parallel-wall waveguide with a centrally located metallic bar. In comparison with other approaches, the method gave satisfactory results. Computer programs were developed for the use of the method and for the comparisons. The study is described in part 8 of the report.

STANDARDIZED NOTATIONS RELATED TO WIRE GRIDS

Z_p, Z_{wo} . . . . . Impedance of wire grid itself without losses (reactive part).

Z_{wo} . . . . . Contribution to wire-grid impedance by conduction losses of wires.

Z_w . . . . . Total impedance of wire grid.

Z_s . . . . . Surface impedance taking into account radiation through the grid.

s . . . . . Spacing between axes of wires.

d . . . . . Diameter of wires.

$t = s/d - 1$ Geometry parameter.

$p = Im[Z_w/Z_o]$ Normalized reactance.

$q = Re[Z_w/Z_o]$ Normalized resistance.

$[Z_w/Z_o = jp + q]$

N70-36440

Reprinted from IEEE TRANSACTIONS
ON *MICROWAVE THEORY AND TECHNIQUES*
Volume-MTT-18, Number 1, January, 1970
pp. 9-15
COPYRIGHT © 1970—THE INSTITUTE OF ELECTRICAL AND ELECTRONICS ENGINEERS, INC.
PRINTED IN THE U.S.A.

H Guide with Laminated Dielectric Slab

FREDERICK J. TISCHER, FELLOW, IEEE

Abstract—A consideration of the field distribution and the characteristics of an *H* guide with a laminated dielectric bar composed of an arbitrary number of dielectric strips separated by air layers is presented. Low-loss wave modes with the electric field intensity predominantly parallel to the sidewalls are analyzed. Approximate thin-layer equations are derived which indicate methods for improvements of the attenuation of the *H* guide.

INTRODUCTION

THE *H* guide is a hybrid waveguide in which the fields are concentrated in one transverse direction by surface-wave guidance and are confined in the other direction by parallel conducting planes. The cross section has the form of an *H* with the conducting side walls forming its vertical legs and the dielectric slab the horizontal bar. The guide has low conduction losses in the walls for wave modes with the electric field strength predominantly parallel to the sidewalls, similar to those of the waveguide with circular cross section for TE_{10} waves. Since the major contributions to the attenuation of the waveguide result from the dielectric losses, lamination of the dielectric bar was proposed [1] to reduce these dielectric losses. Computation and measurement of the characteristics of a double-strip *H* guide confirmed the feasibility of improving the loss characteristics by this approach [2], [3], [6].

This paper presents the derivation of the field distribution and of characteristic data for an *H* guide with the dielectric bar subdivided into an arbitrary number of dielectric strips separated by air layers. The resulting relationships can be drastically simplified in the case of thin strips. Under these conditions, the slab structure may be considered as an artificial dielectric with an equivalent permittivity ϵ_{req} and loss

Manuscript received January 10, 1969; revised July 7, 1969. This work was supported in part by NASA Grant NGR 34-002-47.

The author is with the Department of Electrical Engineering, North Carolina State University, Raleigh, N. C. 27607.

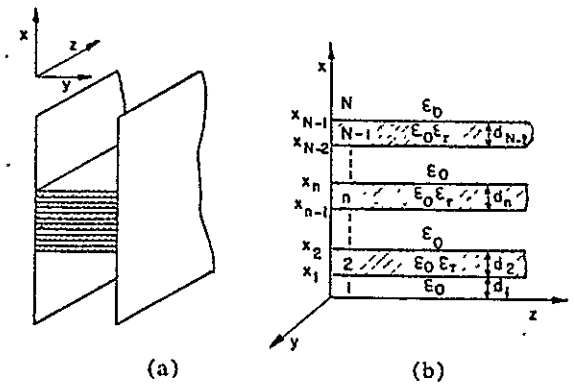

(a) (b)

Fig. 1. *H* guide with laminated dielectric. (a) Cross section of the guide. (b) Laminated-slab structure.

tangent tan δ_{eq}. Diagrams are presented which show the attainable improvements in the loss characteristics of the guide resulting from the lamination. Low-loss wave modes with the *E* field in the center of the guide parallel to the side walls are considered.

Method of Derivation

The method of deriving relationships for the laminated *H* guide is based on the concept that the fields in a parallel-wall waveguide can be considered as those of superimposed plane waves bounced back and forth between the conducting walls. Applying this approach to the present case, the analysis can be carried out in two steps. First, surface-wave propagation along an infinite slab of a laminated dielectric is considered, and then two plane surface waves are superimposed to form the field within the *H* guide.

The structure under investigation is illustrated in Fig. 1(a) for the example of a slab composed of six dielectric strips. Since the distributions of the field components are symmetrical and antisymmetrical with regard to the horizontal center planes, it is sufficient to consider the fields in the upper half of the guide, as if a perfectly conducting electric or magnetic wall separated the upper from the lower half.

The outlined method of derivation hence suggests as a first step the derivation of relationships for the surface-wave propagation along the laminated infinite dielectric slab. Its structure, representing only the upper half, is indicated in Fig. 1(b). It consists of N layers consisting alternately of dielectric and air. In reality, the slab may be composed of high-permittivity dielectric strips separated by layers of foam material with low permittivity and low loss. The dielectric strips have equal thicknesses d_a, characteristics ϵ_r, and separations d_a.

Wave Propagation Along a Laminated Dielectric Slab

Wave propagation along a laminated dielectric slab was considered by Mathis [4] who used a transmission-line approach for the determination of the propagation characteristics. This approach will be used in a modified form for deriving the field distribution in the slab structure of Fig. (b). The wave fields are described in rectangular coordinates as solutions of the wave equation. The magnetic field strength, which is parallel to the boundary surfaces (TM), and the other field components have in customary notation the following form for waves propagating in the positive z direction:

$$H_y^{(n)} = \{A_n \exp[-\gamma_{xn}(x - x_{n-1})] + B_n \exp[+\gamma_{xn}(x - x_{n-1})]\} e^{-jk_z z}, \quad (1a)$$

$$E_x^{(n)} = \frac{j}{\omega\epsilon}\frac{\partial H_y^{(n)}}{\partial z} = (k_z/\omega\epsilon)H_y^{(n)}, \quad (1b)$$

$$E_z^{(n)} = -\frac{j}{\omega\epsilon}\frac{\partial H_y^{(n)}}{\partial x} = (j\gamma_{xn}/\omega\epsilon)\{A_n \exp[-\gamma_{xn}(x - x_{n-1})] - B_n \exp[+\gamma_{xn}(x - x_{n-1})]\} e^{-jk_z z}. \quad (1c)$$

The propagation constants are related in air by

$$\gamma_{xn} = \alpha_x;\ \alpha_x^2 = k_z^2 - k_0^2;\ k_z > k_0;\ k_0 = \omega\sqrt{\epsilon_0\mu_0}, \quad (2a)$$

and in dielectric by

$$\gamma_{xn} = jk_x;\ k_x^2 = k_0^2\epsilon_r - k_z^2;\ k_z < k_0\sqrt{\epsilon_r}. \quad (2b)$$

Summation of the equations for α_x^2 and k_x^2, (2a) and (2b), yields

$$\alpha_x^2 + k_x^2 = k_0^2(\epsilon_r - 1), \quad (3)$$

which is one of the basic equations describing the propagation characteristics of the surface waves.

The field distribution in region 1 ($n=1$) for magnetically symmetric wave modes is found from (1) by introducing the boundary condition $E_z=0$ for $x=0$. In customary notation,

$$H_y^{(1)} = 2A_1 \cosh \alpha_x x,$$
$$E_x^{(1)} = (k_z/\omega\epsilon_0)2A_1 \cosh \alpha_x x, \quad (4)$$
$$E_z^{(1)} = -j(\alpha_x/\omega\epsilon_0)2A_1 \sinh \alpha_x x.$$

The corresponding equations for electrically symmetric (odd) modes ($H_y=0$ for $x=0$) are found to have cosh $\alpha_x x$ and sinh $\alpha_x x$ of (4) interchanged. The fields in dielectric region 2 are given by

$$H_y^{(2)} = \{A_2 \exp[-jk_x(x - x_1)] + B_2 \exp[+jk_x(x - x_1)]\},$$
$$E_x^{(2)} = (k_z/\omega\epsilon_0\epsilon_r)H_y^{(2)}, \quad (5)$$
$$E_z^{(2)} = -(k_x/\omega\epsilon_0\epsilon_r)\{A_2 \exp[-jk_x(x - x_1)] - B_2 \exp[+jk_x(x - x_1)]\}.$$

The constants A_2 and B_2 can be found in terms of A_1 for even and odd modes by equating the tangential field components $H_y^{(1)}$, $E_z^{(1)}$ and $H_y^{(2)}$, $E_z^{(2)}$ at the boundary at $x=x_1$. Equating the field components at the next higher order boundary and subsequent repetition yields the constants A_n and B_n and after insertion into (1) the field components in terms of the amplitudes of the field components at the lower boundary in the center of the guide at $x=0$. In the uppermost air region which extends to $x=\infty$, the field components are, since $B_N=0$, given by

$$H_y^{(N)} = A_N \exp\left[-\alpha_x(x - x_{N-1})\right],$$
$$E_x^{(N)} = (k_z/\omega\epsilon_0)H_y^{(N)}, \tag{6}$$
$$E_z^{(N)} = j(\alpha_x/\omega\epsilon_0)A_N \exp\left[-\alpha_x(x - x_{N-1})\right].$$

The derived equations show that the field distributions are sinusoidal in the x direction in the dielectric strips and are described by hyperbolic functions in the air layers. The hyperbolic functions indicate the surface-wave character in the air layers. In the air region above the laminated structure, the field decreases exponentially toward infinity, assuming infinitely wide strips.

The multiple-layer structure according to Fig. 1(b) and the form of (1) suggests derivation of recursion equations which express the field amplitudes at each upper boundary of a layer in terms of those at the next lower boundary. Considering only components in the directions transverse to x, we find from (1)

$$H_y^{(n)}(x_n) = H_y^{(n-1)}(x_{n-1}) \cos k_x d_n + j \frac{1}{Z_{pe}} E_z^{(n-1)}(x_{n-1}) \sin k_x d_n, \tag{7a}$$

$$E_z^{(n)}(x_n) = Z_{pe} H_y^{(n-1)}(x_{n-1}) j \sin k_x d_n + E_z^{(n-1)}(x_{n-1}) \cos k_x d_n. \tag{7b}$$

The equations are similar to those for current and voltage at the input and output of sections of transmission lines. Hence, the field distribution in the x direction can be considered by transmission-line methods as indicated by Mathis. According to the transmission-line concept, a transverse impedance can be defined as $Z^{(n)} = E_z^{(n)}/H_y^{(n)}$ which can be expressed by familiar relationships as a function of $Z^{(n-1)}$ with Z_{pe}, k_x, and d_n as parameters. The latter describe the characteristics of the nth layer, where

$$Z_{pe} = \frac{1}{\epsilon_r} \frac{k_y}{k_0} Z_0; \qquad Z_0 = \frac{\mu_0}{\epsilon_0}. \tag{8}$$

Similar equations involving hyperbolic functions govern the relationship between the various quantities in the air layers.

It is convenient to introduce matrix representation for the consideration of the multiple-layer structure. Writing (7) in matrix form, a transmission matrix $[T]$ relates the field quantities. For the nth dielectric layer, it is given by

$$[T^{(n)}] = \begin{bmatrix} \cos k_x d_n & j \dfrac{i}{Z_{pe}} \sin k_x d_n \\ j Z_{pe} \sin k_x d_n & \cos k_x d_n \end{bmatrix}. \tag{9}$$

Transmission in all the layers below can be taken into consideration by writing

$$\begin{bmatrix} H_y^{(n)} \\ E_z^{(n)} \end{bmatrix} = [T^{(n)}][T^{(n-1)}] \cdots [T^{(1)}] \begin{bmatrix} H_y^{(1)}(0) \\ E_z^{(1)}(0) \end{bmatrix}. \tag{10}$$

Taking into account the total number of layers between x_{N-1} and $x=0$, a cumulative transmission coefficient $[T]$ can be defined for the laminated structure:

$$[T] = \begin{bmatrix} T_{11} & T_{12} \\ T_{21} & T_{22} \end{bmatrix} = [T^{(N-1)}][T^{(N-2)}] \cdots [T^{(1)}]. \tag{11}$$

Use of the elements of the matrix T facilitates expressing the transverse wave impedance at the upper boundary of the structure in terms of the fields and impedances at $x=0$:

$$Z_N = \frac{E_z^{(N)}}{H_y^{(N)}} = \frac{T_{21} H_y^{(1)}(0) + T_{22} E_z^{(1)}(0)}{T_{11} H_y^{(1)}(0) + T_{12} E_z^{(1)}(0)}. \tag{12}$$

Substitution of the impedance value Z_N from (6) and of the impedance values at $x=0$ from (4) yields the characteristic equations for the laminated structure:

$$(E_z = 0 \text{ at } x = 0): \quad Z_N = j \frac{\alpha_x}{\omega\epsilon_0} = \frac{T_{21}}{T_{11}}, \tag{13a}$$

for even modes, and

$$(H_y = 0 \text{ at } x = 0): \quad Z_N = j \frac{\alpha_x}{\omega\epsilon_0} = \frac{T_{22}}{T_{12}}, \tag{13b}$$

for odd modes. Inspection of (9), (11), and (13) shows that the characteristic equations describe relationships between k_x and α_x for even and odd modes. In combination with (3), they facilitate the determination of k_x and α_x. The transcendental equations (13) can then be written in a general form as

$$k_x = f_{e,o}(\alpha_x, \epsilon_r, d_\epsilon, d_a) \tag{14}$$

where d_ϵ and d_a are the thicknesses of the dielectric strips and the air layers, respectively. The exact evaluation of the characteristic equations can be carried out for large numbers of layers by computer. An impedance-matching process by the use of the Smith chart outlined by Mathis [4] can be used if the number of layers is small. Approximate relations derived in the next section are satisfactory for many practical cases.

Relationships for Thin Dielectric Slabs

The possibility of simplification of the derived equations for thin layers is explored next since it can be expected that the slabs of the laminated H guide satisfy this condition. Assumption of thin layers, when $\alpha_x d_a$, $k_x d_\epsilon \ll 1$, allows the following approximations:

$$\cos k_x d_\epsilon, \cosh \alpha_x d_a \simeq 1; \sin k_x d_\epsilon \simeq k_x d_\epsilon;$$
$$\sinh \alpha_x d_a \simeq \alpha_x d_a.$$

The approximations are introduced into (7) and (9) and into two representative transmission matrices $T^{(n)}$ and $T^{(n-1)}$ for a pair of layers, one containing air and the other containing a dielectric medium. By matrix multiplication, a new matrix can now be found that describes the transmission through a uniform single layer equivalent to the combined transmission through the two layers. The new transformation matrix is hence given by

$$[T^{(D)}] = \begin{bmatrix} T_{11}^{(D)} & T_{12}^{(D)} \\ T_{21}^{(D)} & T_{22}^{(D)} \end{bmatrix} = \begin{bmatrix} T_{11}^{(n)} & T_{12}^{(n)} \\ T_{21}^{(n)} & T_{22}^{(n)} \end{bmatrix} \begin{bmatrix} T_{11}^{(n-1)} & T_{12}^{(n-1)} \\ T_{21}^{(n-1)} & T_{22}^{(n-1)} \end{bmatrix}. \tag{15}$$

Substitution of the approximate values of the matrix elements into (9) and (15) and carrying out the matrix multiplication yields

$$T_{11}^{(D)} \simeq 1 \simeq 1 - k_x^2 d_e d_\epsilon \frac{1}{\epsilon_r}, \tag{16a}$$

$$T_{12}^{(D)} \simeq j \frac{k_0}{Z_0} \epsilon_{req}(d_\epsilon + d_a) \simeq j \frac{k_0}{Z_0} (\epsilon_r d_\epsilon + d_a), \tag{16b}$$

$$T_{21}^{(D)} \simeq j \frac{Z_0}{k_0} k_{xeq}^2 \frac{(d_\epsilon + d_a)}{\epsilon_{req}} \simeq j \frac{Z_0}{k_0}\left(\frac{k_x^2}{\epsilon_r} d_\epsilon - \alpha_x^2 d_a\right), \tag{16c}$$

$$T_{22}^{(D)} \simeq 1 \simeq 1 + \alpha_x^2 d_e d_\epsilon, \tag{16d}$$

where the permittivity, propagation constant, and thickness of the equivalent single layer are denoted by ϵ_{req}, k_{xeq}, and $d_\epsilon + d_a$, respectively. Evaluating (16b) yields an approximate expression for the equivalent permittivity,

$$\epsilon_{req} \simeq \epsilon_r \frac{1 + p/\epsilon_r}{1 + p}, \tag{17}$$

with $p = d_a/d_\epsilon$ denoting the air-to-dielectric thickness ratio.

Since the characteristics of the equivalent layers are equal, the total laminated dielectric structure can be replaced by a uniform dielectric slab with equal total thickness and having a relative permittivity ϵ_{req}. For thin dielectric layers, the laminated dielectric H guide can thus be treated as a guide with a single slab with an equivalent permittivity given by (17).

Thin-Strip Loss Tangent

Caution is required at the determination of the loss tangent of the equivalent uniform dielectric representing the thin-strip structure. We observe that ϵ_{req} of (17) actually is the real part of the complex equivalent permittivity. It was obtained by considering wave propagation and the field distribution in the x direction and involved E_z and H_y [see (7)]. The imaginary part $\epsilon_{req}''(\epsilon_{req} = \epsilon_{req}' - j\epsilon_{req}'')$ which describes the dielectric losses must be found by a more detailed consideration of the losses and attenuation of the equivalent layer, since the major contribution to the dielectric losses results from E_z which did not appear in the equations from which ϵ_{req}' was derived. This component (E_z) has its maximum value in the center of the slab at $x=0$ for low-loss even modes. At this location the component E_z is zero. Due to the $\sin^2$ distribution of E_z, its contribution to the losses can be neglected in the central region where the dielectric slab is located, and only E_x taken into consideration.

Determination of ϵ_{req}'' will be based on the concept that the attenuation of the equivalent single layer is equal to that caused by dielectric losses in the combination of the original dielectric and air layers. The compared values of attenuation are p_{diss}/p_{trans} which represent the ratios of dissipated and transmitted powers per unit width of the layers. The transmitted power is derived from the z component of the Poynting vector,

$$S_z = \tfrac{1}{2} \operatorname{Re} [E_x H_y^*],$$

which gives for the double layer

$$p_{trans} = \tfrac{1}{2} |H_y|^2 \frac{k_z}{k_0} Z_0 \left(\frac{d_\epsilon}{\epsilon_r'} + d_a\right), \tag{18a}$$

and for the equivalent single layer

$$p_{trans}' = \tfrac{1}{2} |H_y|^2 \frac{k_z}{k_0} \frac{Z_0}{\epsilon_{req}'} (d_\epsilon + d_a). \tag{18b}$$

The dissipated power is derived from

$$p_{diss} = \tfrac{1}{2} |E_x|^2 \sigma_\epsilon d_\epsilon.$$

Substituting H_y for E_x from (5) and $\sigma_\epsilon = \omega\epsilon_0\epsilon_r''$, we find, for the two layers with the dielectric giving a contribution only,

$$p_{diss} \simeq \tfrac{1}{2} |H_y|^2 \frac{k_z^2}{\omega\epsilon_0} \frac{\epsilon_r''}{(\epsilon_r')^2} d_\epsilon, \tag{19a}$$

and for the equivalent single layer,

$$p_{diss}' \simeq \tfrac{1}{2} |H_y|^2 \frac{k_z^2}{\omega\epsilon_0} \frac{\epsilon_{req}''}{(\epsilon_{req}')^2} (d_\epsilon + d_a). \tag{19b}$$

Equating the unprimed and primed ratios of p_{diss}/p_{trans} yields

$$\frac{\epsilon_r''}{\epsilon_r'} \frac{d_\epsilon}{d_\epsilon + \epsilon_r' d_a} = \frac{\epsilon_{req}''}{\epsilon_{req}'},$$

and subsequently for the equivalent loss tangent

$$\tan \delta_{eq} = \epsilon_{req}''/\epsilon_{req}' \simeq \frac{\tan \delta}{1 + p\epsilon_r'}. \tag{20}$$

It is interesting that the validity of (20) can be checked by considering a capacitor with a laminated dielectric with the boundary planes parallel to the capacitor plates. The equation for the equivalent loss tangent is found to be identical to that of (20) for low-loss materials.

Fields in the Laminated H Guide

The fields in the H guide are found by superposition of two plane surface waves propagating along the infinite laminated slab discussed in the preceding sections. One of these waves travels toward the sidewall incident at a finite angle from the normal; the other, the reflected wave, travels toward the center of the guide. The geometries of the directions of waves are shown in Fig. 2. After a change of notation, the field components previously denoted by H_y and E_x are now called the transverse components H_t and E_t of the plane surface waves. The component E_z becomes the longitudinal component E_l. Hence,

$$H_y \to H_t; \quad E_x \to E_t; \quad E_z \to E_l; \quad k_z \to k_l. \tag{21}$$

By use of the geometric relationships indicated in Fig. 2, we express the field components in the coordinate system of the H guide [see Fig. 1(a)] as a superposition of incident ($e^{+jk_y y}$) and reflected waves ($e^{-jk_y y}$); hence, omitting the common term $e^{-jk_z z}$, the field components are

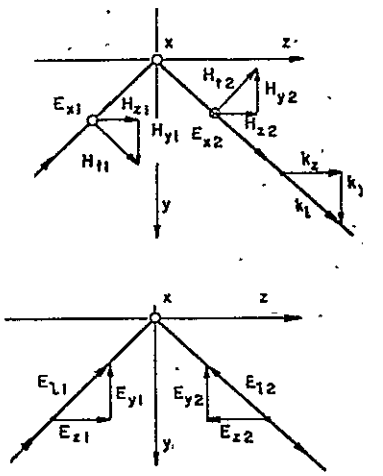

Fig. 2. Geometric relations of the field components of incident and reflected waves at the wall of the guide.

$$
\begin{aligned}
H_z &= H_t(k_y/k_t)(e^{jk_yy} + e^{-jk_yy}) = 2H_t(k_y/k_t)\cos k_yy,\\
H_y &= H_t(k_z/k_t)(e^{jk_yy} - e^{-jk_yy}) = 2H_t(k_z/k_t)]\, j\sin k_yy,\\
E_x &= E_t(e^{jk_yy} - e^{-jk_yy}) = 2E_tj\sin k_yy,\\
E_y &= -E_t(k_y/k_t)(e^{jk_yy} + e^{-jk_yy})\\
&= -2E_t(k_y/k_t)\cos k_yy,\\
E_z &= E_t(k_z/k_t)(e^{jk_yy} - e^{-jk_yy}) = 2E_t(k_z/k_t)j\sin k_yy.
\end{aligned}
\tag{22}
$$

Substitution of the field components for the infinite laminated slab described by (4) through (7) into (22), after taking into account the changes of notations expressed by (21), gives the field distributions in the corresponding layer within the *H* guide. For the *n*th layer which contains dielectric material, the field components are

$$
\begin{aligned}
H_x^{(n)}(x) &= \frac{k_y}{k_t}[U_nc(x) + jV_ns(x)]\cos k_yye^{-jk_zz},\\
H_y^{(n)}(x) &= j\frac{k_z}{k_t}[U_nc(x) + jV_ns(x)]\sin k_yye^{-jk_zz},\\
E_z^{(n)}(x) &= \frac{k_t}{\omega\epsilon_0\epsilon_r}[U_nc(x) + jV_ns(x)]\sin k_yye^{-jk_zz},\\
E_y^{(n)}(x) &= \frac{k_x}{\omega\epsilon_0\epsilon_r}\frac{k_y}{k_t}[V_nc(x) - jU_ns(x)]\cos k_yye^{-jk_zz},\\
E_x^{(n)}(x) &= -j\frac{k_x}{\omega\epsilon_0\epsilon_r}\frac{k_z}{k_t}[V_nc(x) - jU_ns(x)]\\
&\quad\cdot\sin k_yye^{-jk_zz}.
\end{aligned}
\tag{23}
$$

The functions $c(x)$ and $s(x)$ stand for $\cos k_x(x-x_{n-1})$, and $\sin k_x(x-x_{n-1})$, respectively. The constants $U_n=(A_n+B_n)/2$ and $V_n=(A_n-B_n)/2$ are proportional to the field components E_x and E_z at the lower boundary of the region n. The corresponding equations for an air layer are found by substituting hyperbolic functions for the trigonometric functions $c(x)$ and $s(x)$, $\epsilon_r=1$, and $-j\alpha_x$ for k_x.

Mode Analysis

Confinement of the waveguide fields in the y direction by the conducting walls is associated with an infinite spectrum of higher order wave modes. The boundary conditions, $E_z=0$ at $y=0$, a, require that $k_{ym}=m\pi/a$. Since the longitudinal propagation constant k_t is related to its components by $k_t^2=k_y^2+k_z^2$ (Fig. 2), the propagation constants in the various directions are interrelated by

$$k_0^2\epsilon_r = k_x^2 + k_{ym}^2 + k_{zm}^2 \tag{24a}$$

in dielectric, and

$$k_0^2 = -\alpha_x^2 + k_{ym}^2 + k_{zm}^2 \tag{24b}$$

in air. In a waveguide of proper width, only the fundamental mode is propagating and the higher order modes are evanescent with the fields decreasing exponentially in the z direction with negligible phase shift.

The constants α_x and k_z which describe the field distribution and the surface-wave character in the x direction can be computed from (3) and (14):

$$k_x^2 = k_0^2(\epsilon_r - 1) - \alpha_x^2, \tag{25a}$$

$$k_x^2 = f_{e,o}(\alpha_x, \epsilon_r, d_a, d_\epsilon), \tag{25b}$$

which are the characteristic equations for the infinite laminated slab. The relationships are not affected by the confinement by the two parallel walls and are valid for the *H* guide also. Excitation of the even and odd modes with different distributions in the x direction depends on the operational frequency, the permittivity of the strips, and the geometry of the laminated structure. The fundamental magnetically odd wave mode (even with regard to E_x) can always be excited since its existence is frequency-independent. The higher order modes with multiple periodicities in the x direction in the slab and all magnetically even modes have cutoff frequencies as lower limits for their existence. The propagation characteristics are basically similar to those of surface waves along an infinite solid dielectric slab [5]. The similarity becomes particularly pronounced in the case of

thin layers of the dielectric and air for which the approximate relationships derived previously can be used. Denoting the single or multiple solutions of the equation pair (25) by k_{xq}, which have to be found for the specific operational conditions, the propagation constant in the z direction becomes

$$k_{zm,q}^2 = k_0^2 \epsilon_r - k_{xq}^2 - \left(\frac{m\pi}{a}\right)^2. \tag{26}$$

Equation (25b) has to be solved for thick layers by computer; for a small number of strips, it can be solved by the impedance-matching process outlined by Mathis. In the case of thin layers the substitution by a uniform dielectric slab with an equivalent permittivity can be applied. Basically the excitation of waveguide modes in the laminated waveguide is similar to that in the H guide with a single solid slab described previously.

Improvement of Loss Characteristics by Lamination

The study of the two-strip H guide has shown that the attenuation has a general trend to decrease with decreasing thickness of the dielectric slabs [2], [3]. The same trend can be observed in the case of the laminated guide with thin dielectric strips. It can hence be expected that a considerable reduction of the attenuation can be achieved by lamination of the dielectric slab and by reducing the thickness of the dielectric strips. Due to these trends the thin-strip approximation should give satisfactory results in a consideration of the attenuation of the laminated H guide.

The major contribution to the attenuation of an H guide at millimeter waves of nonexcessive size results at present from dielectric losses. Information with regard to the reduction of the attenuation can be gained by evaluating and comparing the dielectric losses of various structures disregarding the effects of differences of the geometries on the wall losses. If the equivalent permittivities of the compared slabs are kept constant, the disregard of geometric changes is well justified. The relationships derived for thin layers will be used for such an evaluation next.

The dielectric losses in the guide are directly proportional to the loss tangent (tan δ) of the medium of the strips. A reduction of tan δ is hence the primary source of a reduction of the attenuation. The equation which shows the feasibility for such a reduction is (20),

$$\tan \delta_{eq} = \tan \delta/(1 + \epsilon_r p); \qquad p = d_a/d_\epsilon.$$

It should be noted that this equation involves primarily the electric field component E_x which contributes to the transmission of power along the guide. It has a maximum amplitude in the center of the guide where the dielectric is located. The other components E_y and E_z are zero at $x=0$ [see (4)] and can thus be disregarded in the approximation. The second important equation involves the equivalent permittivity

$$\epsilon_{req} = \epsilon_r(1 + p/\epsilon_r)/(1 + p).$$

Graphical representations of the two relationships are shown

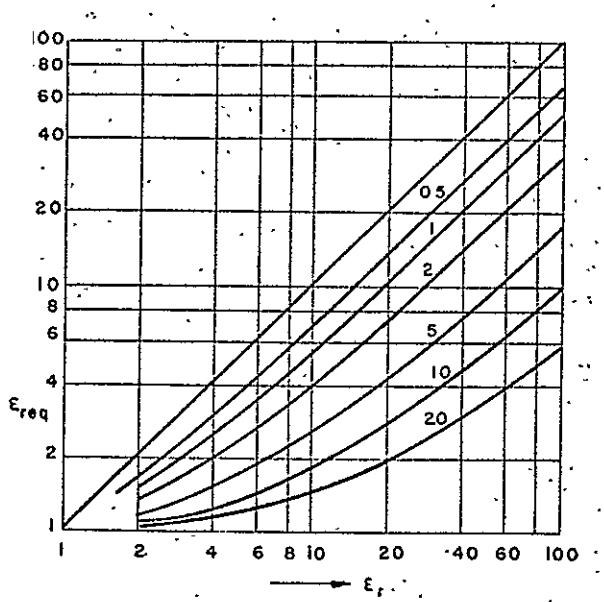

Fig. 3. Equivalent permittivity of the laminated dielectric slab.

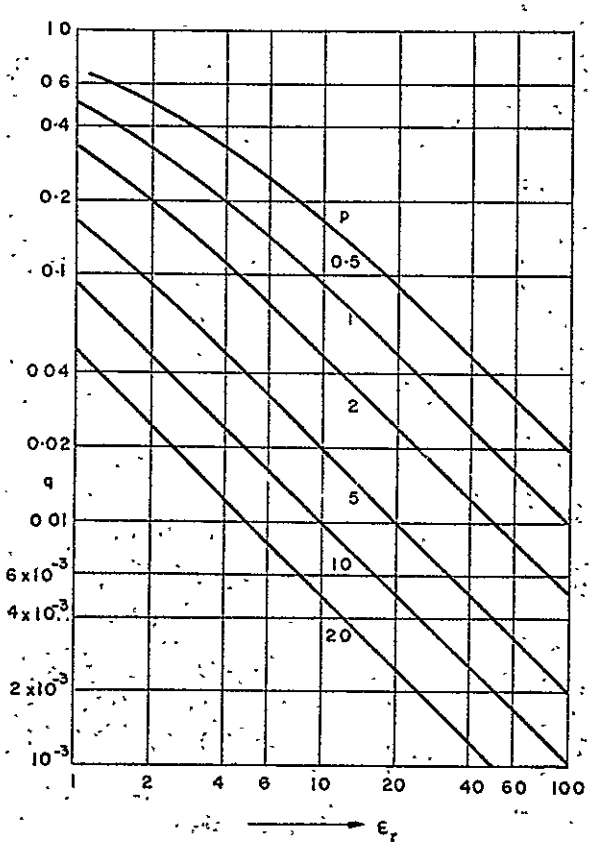

Fig. 4. Reduction factor of loss tangent of the laminated dielectric slab ($q = \tan \delta_{eq}/\tan \delta_{strip}$).

in Figs. 3 and 4. The preceding considerations indicate that a considerable reduction of the attenuation of the H guide can be expected at millimeter waves if tan δ_{eq} can be reduced by choice of proper materials and geometry p of the laminated structure while keeping ϵ_{req} constant. The equations indicate that dielectrics with high permittivity at low dielectric losses and lamination with a high value of p are best suited for a reduction of attenuation. The comparison of loss

TABLE I

Dielectric	Single-Slab Parameters		Laminated-Slab Parameters		
	ϵ_r	tan δ	p	ϵ_{req}	tan δ_{eq}
Styrofoam	1.03	1.5×10^{-4}			
Rexolite	2.53	7×10^{-4}*	7.5	1.16	3.5×10^{-5}
Beryllium Oxide (99.5%)	6.6	4.4×10^{-4}	3	2.4	2.6×10^{-5}
Aluminum Oxide (99.9%)	9.9	2.5×10^{-5}	5	2.5	5×10^{-7}
Eccoceram	90	1.0×10^{-3}	10	9	1.1×10^{-6}

* At 24 GHz, others at 10 GHz.

tangents and permittivities in Table I shows that equivalent loss tangents in the guide obtained by lamination are considerably superior to those of dielectrics in the single-slab guide. It seems that a reduction of the loss tangent by one order of magnitude is possible.

Conclusions

Wave propagation in an infinite laminated slab has been considered as a first step of an analysis of the laminated H guide. Equations for the field distributions in the various regions of a multiple-layer structure have been presented and characteristic equations for the total structure derived. Matrix representation was found most useful for describing the characteristics of the multiple structure for even and odd wave modes. The infinite-slab consideration represents the first part. In the second part, the H guide fields are derived by superposition of two infinite-slab surface waves incident and reflected from one of the two parallel conducting sidewalls. This approach simplifies considerably the derivation of the field equations. The subsequent analysis of the wave modes shows that the wave modes have basically the same characteristics as those of the single-slab guide.

Thin-layer approximations allow considerable simplifications of the derived equations. They facilitate simple consideration of the laminated structure by an equivalent single layer of a medium with an equivalent permittivity and loss tangent. Emphasis is then placed on an evaluation of the equivalent loss tangent in a thin-layer structure since it indicates clearly the methods by which the attenuation of the guide can be reduced particularly in the millimeter-wave region. The equations, the graphs, and a comparison of the equivalent loss tangents for various materials show that use of low-loss high-permittivity materials and combination with thin-strip lamination give considerable reductions of the dielectric losses which in turn lead to considerable improvements of the attenuation of the H guide.

References

[1] F. J. Tischer, "A waveguide structure with low losses," *Arch. Elec. Übertragung*, vol. 7, pp. 592–596, December 1953.
[2] ——, "Properties of the H guide at microwaves and millimeter waves," *Proc. IEE* (London), vol. 106B, suppl. 13, pp. 47–53, January 1959.
[3] R. F. B. Conlon and F. A. Benson, "Propagation and attenuation in the double-strip H guide," *Proc. IEE* (London), vol. 113, pp. 1311–1320, August 1966.
[4] H. F. Mathis, "How surface waves propagate along a dielectric sandwich," *Electronics*, p. 82, May 1961.
[5] R. F. Harrington, *Time-Harmonic Electromagnetic Fields*. New York: McGraw-Hill, 1961, sect. 4-7.
[6] Y. D. Deniskin, "Metal-dielectric H-guide with two dielectric slabs," *Telecommun. Radio Engrg.*, vol. 18, pp. 37–46, 1963.

N70-36441

RESULTS OF LIGHT REFLECTANCE MEASUREMENTS FROM ROUGH SURFACES

Introduction

In a study of the effects of surface roughness on the loss characteristics of waveguides and cavities at millimeter waves, optical methods are used for the determination of the surface roughness.

It is well known that light is reflected from metallic surfaces but the reflection phenomena are still being investigated. If the metallic surface is polished to a mirror-like finish, light is reflected at an angle to the normal equal to the incident angle. However, for a surface containing irregularities, the reflected light contains both specular and diffused parts. The specular light is reflected as previously stated but the diffused light is scattered in all directions. As the roughness of the surface increases, then for the same incident light the intensity of specular reflection decreases while the diffused increases. For near normal incident light it has been observed that the diffused light intensity with angular displacement about the specular angle appears to have a Gaussian distribution. From experimental data the spread or variance of this distribution is observed to be dependent on the "roughness" of the surface. This paper is a description of the preparation of the surfaces, the equipment used to measure the reflectance, and preliminary data reduction. A microscopic analysis of the surface is in progress and will be presented later.

Sample Preparation

Since the final goal is to determine the contribution of surface roughness to attenuation in waveguides, the metal chosen was copper. A sheet of 1/8" copper was cut into $1\frac{1}{2}$ by 2 inch sections. This size was selected for ease of handling as well as constraints imposed by the reflectance measuring equipment.

Grinders manufactured by Buehler Ltd. were available and could be used to prepare the samples. There were two types of grinders; one consisted of a set of abrasive papers mounted on hard, flat surfaces and the other having the same type of mounting but a continuous flow of water immediately washed away the loose abrasive material and fragments of the metal. These metallurgical grinders, both the dry and wet, were used for preliminary preparation in polishing of metal surfaces.

The copper surfaces were prepared in the following manner. First, the sample was moved forth and back on the coarsest grade of paper until grooves were present in only one direction. It was important that the grooves appear in only one direction since the finer paper can only remove the grooves created by the next coarser paper. The force on the samples was held to a minimum to prevent crushing the abrasive particles which could cause large variation in the grooves and cause smoother surfaces than intended. The force was only that to keep the samples in a position to create parallel grooves. The sample was then rotated ninety degrees and placed on the next finer paper. The process was continued until the desired degree of polishing was obtained. In our investigation, six grades of abrasive paper were used. The grain size of each abrasive paper

is given in table 1.

After each grinding the samples were rinsed under running water to remove loose material from the surface. A stream of air with sufficient force was blown across the surface to rapidly remove residual water and thus minimize water spots. The surfaces were carefully handled to prevent finger prints or other stains and were stored in a cabinet until reflectance studies could be made.

Reflectance Setup

The reflectance measurement setup is illustrated in Fig. 1a,b. The light source is a Spectra-Physics Model 124 Helium-Neon Laser capable of supplying fifteen milliwatts of power at 6328 Å. An adjustable attenuator with degree indicators along the circumference is used to regulate the light intensity that strikes the test sample. The relative attenuation can be determined by the angular displacement from a reference when applied to the sin square law. A continuous monitor of the source intensity is accomplished by a beam splitter which deflects part of the light into a Spectra-Physics 401 C power meter. If variations should occur during an experiment the attenuation can be adjusted to correct the change. A flat, circular disc with a mounting stand located in the center is used to secure the test sample. The five inch radius disc has degrees marked off around the perimeter and with aid of markers, the angles of incidence and reflectance can be measured. An extension arm which pivots about the center of the disc holds a light detector which consists of an RCA 7102 multiplier phototube and associated circuitry.

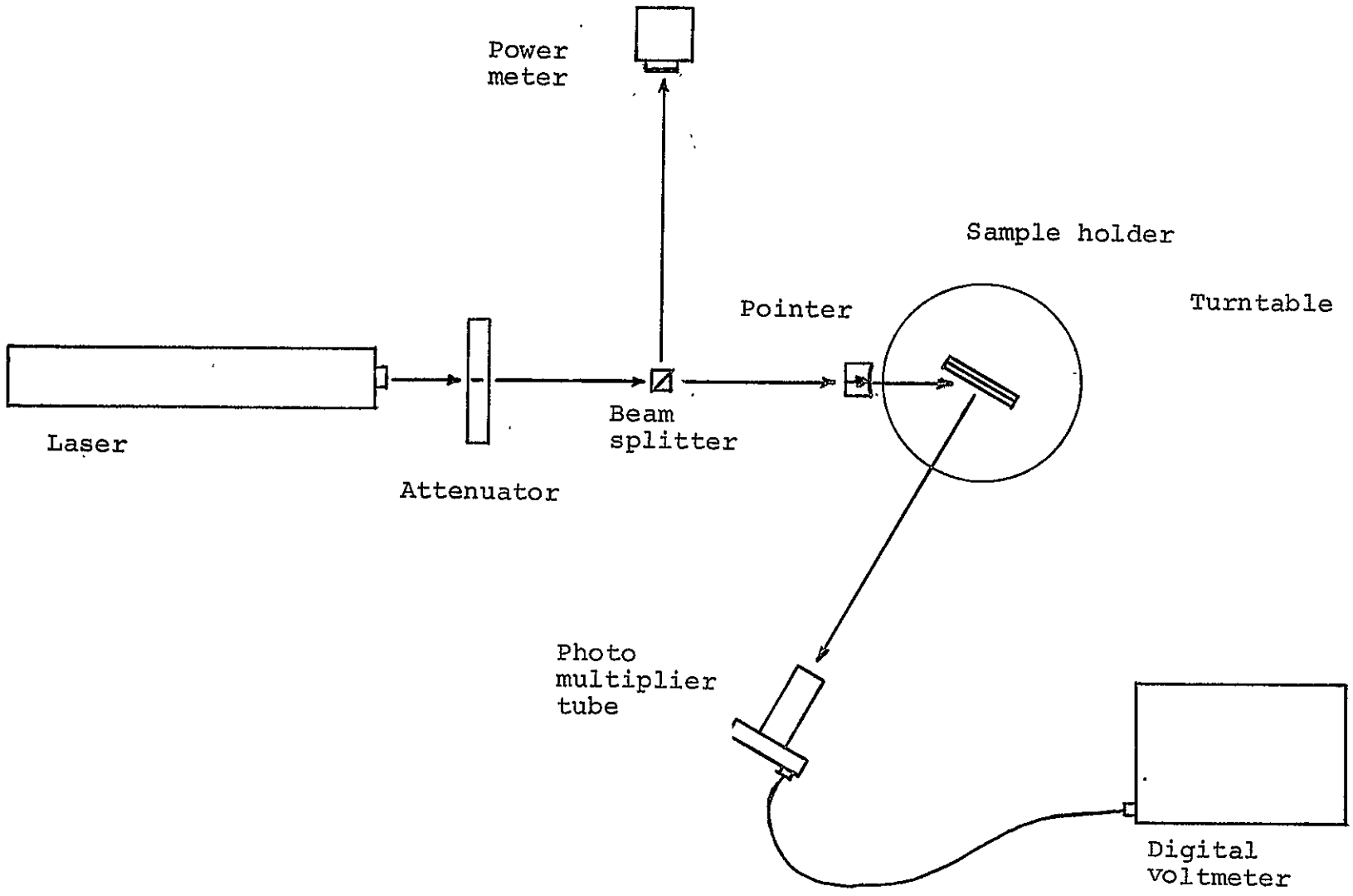

Fig.1a Reflectance measurement setup

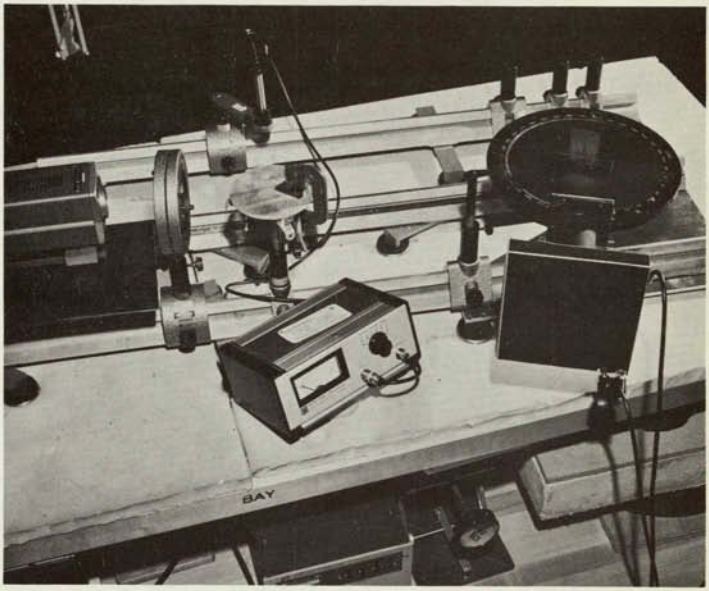

Fig. 1b Photograph of reflectance measurement setup

Table 1

Abrasive Paper Particle Size

Grade	Grain size in microns
Emery 2	62
Emery 1	38
Grit 240	48
Grit 320	30
Grit 400	24
Grit 600	15

The photo tube is enclosed in a light tight cover with a one-eighth by one inch slit. The extension arm maintains the slit at a constant distant from the center of the disc and at a constant height above the plane of the disc. The power for the multiplier is supplied by a Hewlett-Packard Harrison 6516A DC power supply and the output of the detector is displayed on a Doric Integrating Microvoltmeter. The assembly, with the exception of the power supplies and the voltmeter, is mounted on an optical rail which permits accurate alignment of the various components. The entire setup is located in a dark room whose walls have been sprayed with a non-glossy black paint.

Three sets of experimental data were taken from the setup. For the first experiment, the angle of incidence and incident light were held constant, and in a plane perpendicular to surface, the reflected light was measured at angles from the surface normal between 0 and 90 degrees. During the second experiment, the incident angle was held constant and the light reflectance was measured at the specular angle for various intensities of incident light. For the final experiment the incident light was held constant and the incident angle was varied between 10 and 90 degrees while the reflectance was measured at the specular angle. These measurements were taken for each of the test samples and is given in the next section.

Results

The data were plotted as three separate graphs and are shown in Figs. 2, 3, and 4. Figure 2 is a plot of the normalized reflectance versus angular displacement from the surface normal for

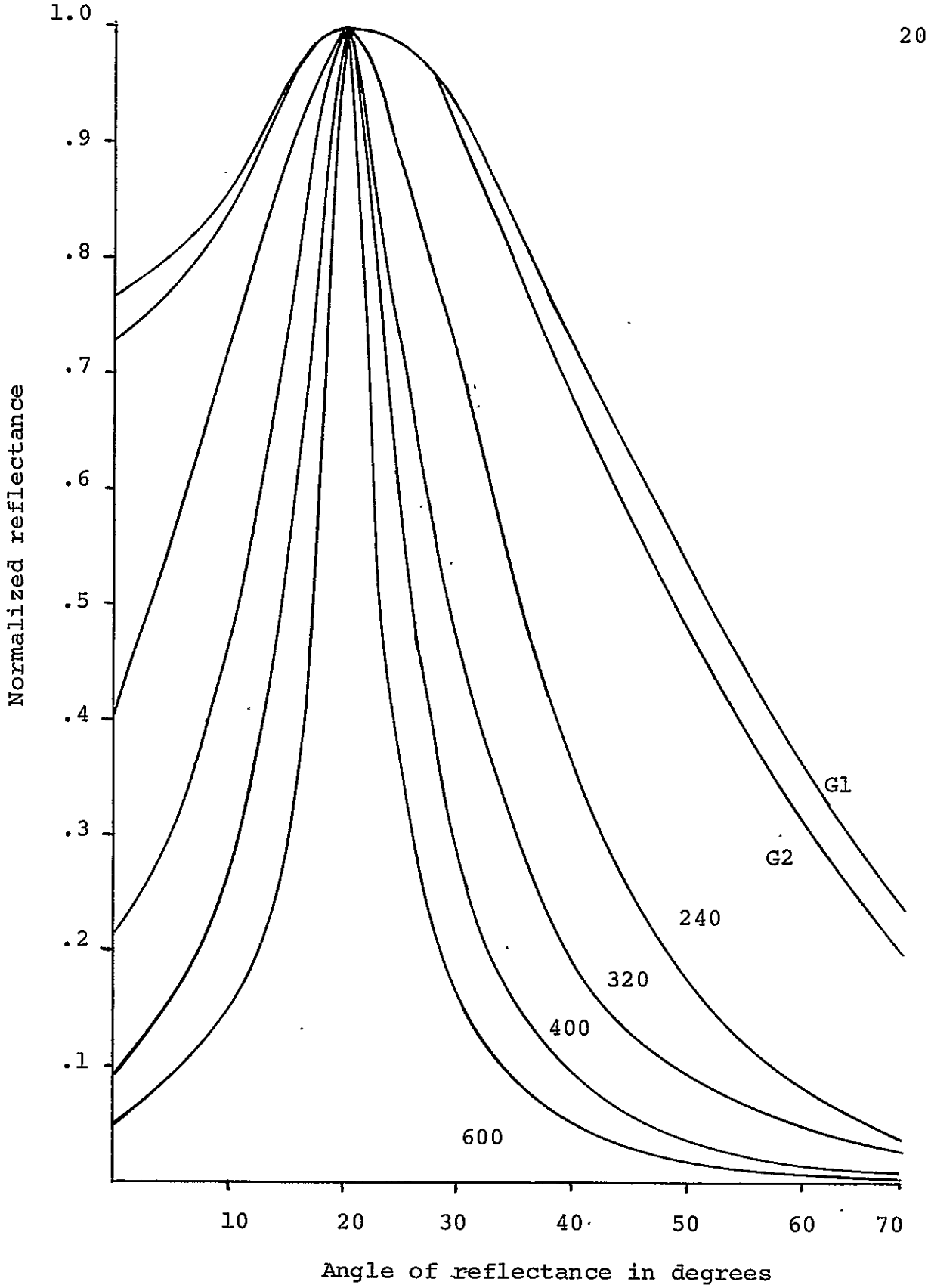

Fig. 2. Reflectance of rough surfaces averaged and normalized with regard to maximum versus angle of reflectance for constant angle of incidence

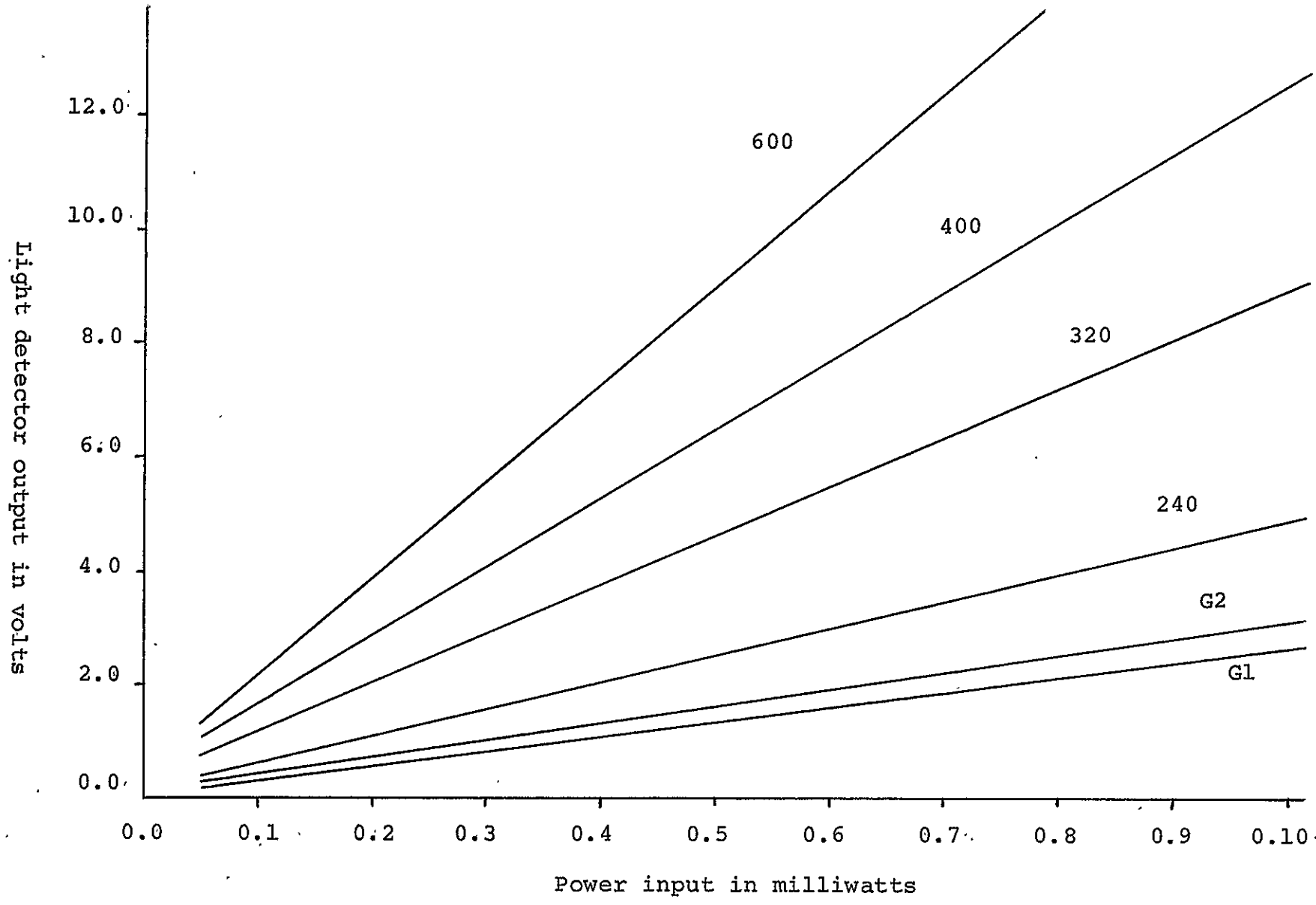

Fig. 3 Light intensity (relative) reflected from rough surfaces versus incident light power. Angles of incidence and reflectance were equal and kept constant.

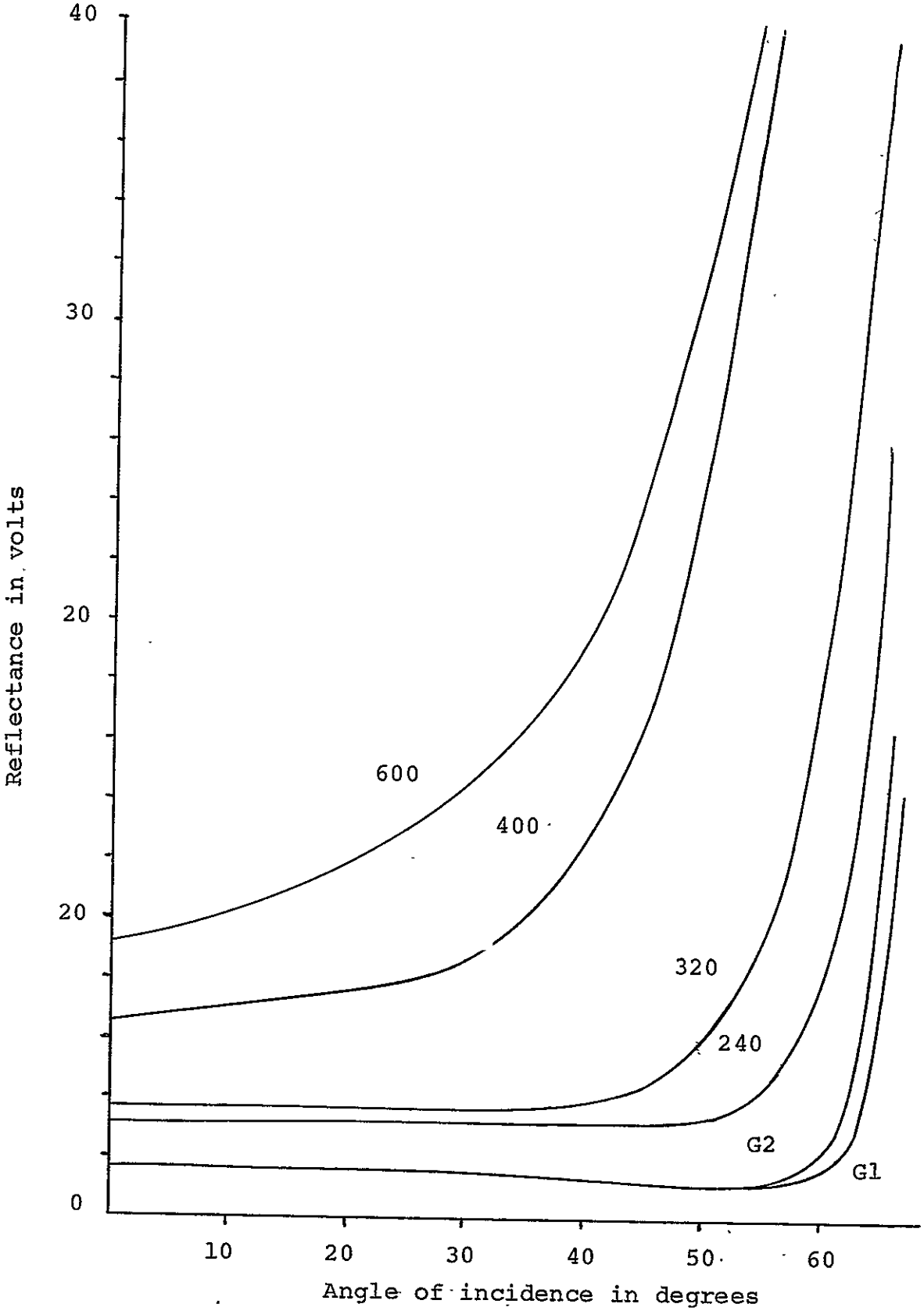

Fig. 4 Reflectance of rough surfaces versus angle of incidence for angle of reflectance equal to the angle of incidence

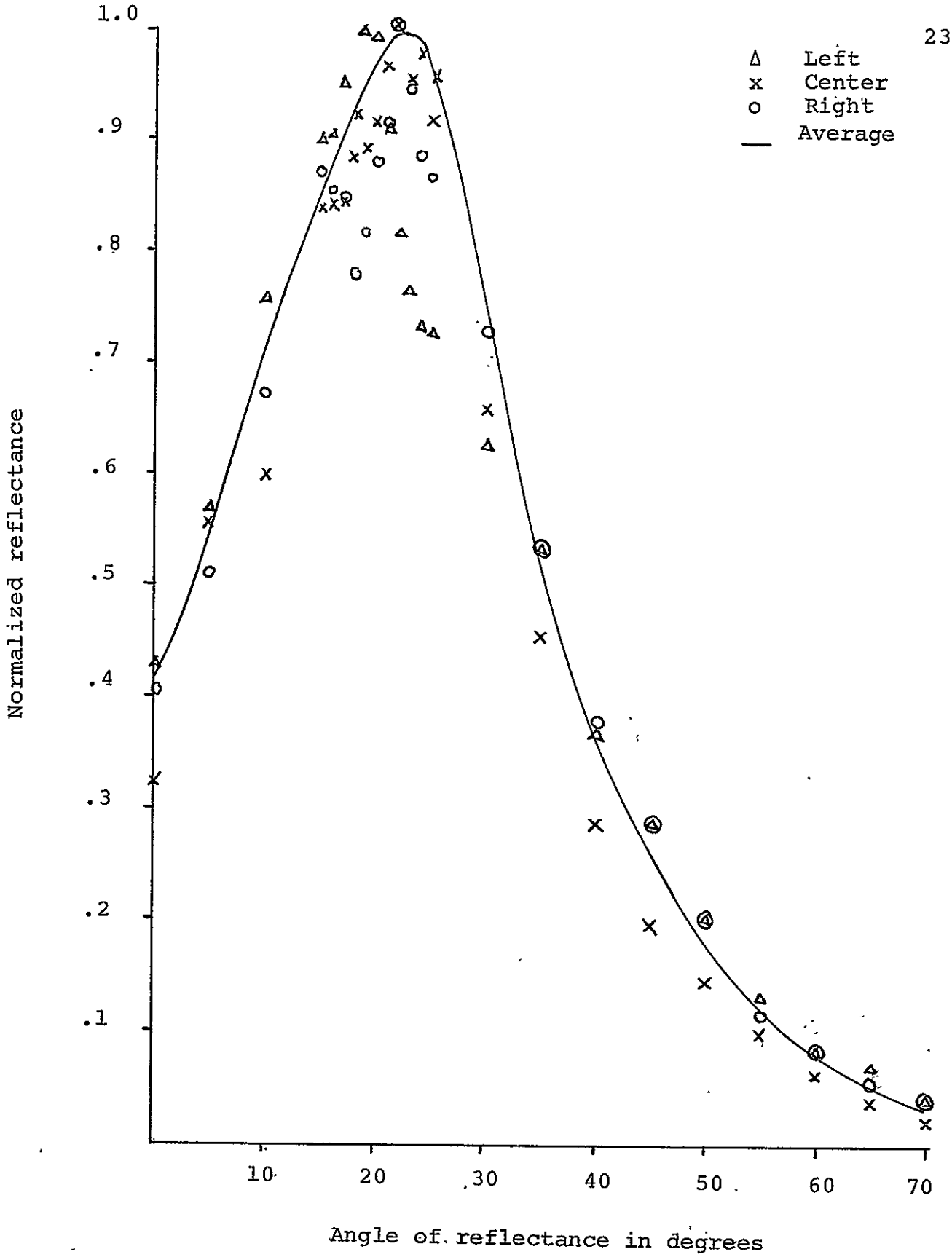

Fig. 5 Individual measurement results which form the basis of the averaged reflectance curves of Fig. 2.

the case where the incident light and angle are held constant. The curves for each test sample are the results of averaging of three locations on the sample. The locations are the center and 1/4 inch on each side of the center. Figure 5 shows the variation and how the different locations relate to the average. The curves appear symetrical about the specular angle and resemble Gaussian curves. The coarser the abrasive paper the broader is the spread or variance of the curve.

Figure 3 shows a plot of specular reflectance versus incidence light for a constant angle of incidence. Each set of data gives a linear curve. For these cases the coarser the abrasive paper the smaller the amplitude of the reflected light and the greater the slope.

Figure 4 illustrates the dependence of roughness on the angle of incidence. The graphs are plots of the specular reflection versus the incident angle for the case of constant incident light. The expected result would be that at some angle the surface would reflect more light than nearer the normal and would increase its reflectance until the grazing angle was obtained. This was verified because the finer the abrasive paper used the sooner the increase began and the greater the slope of the curve.

Discussion:

The model used in this section is shown in Fig. 6.

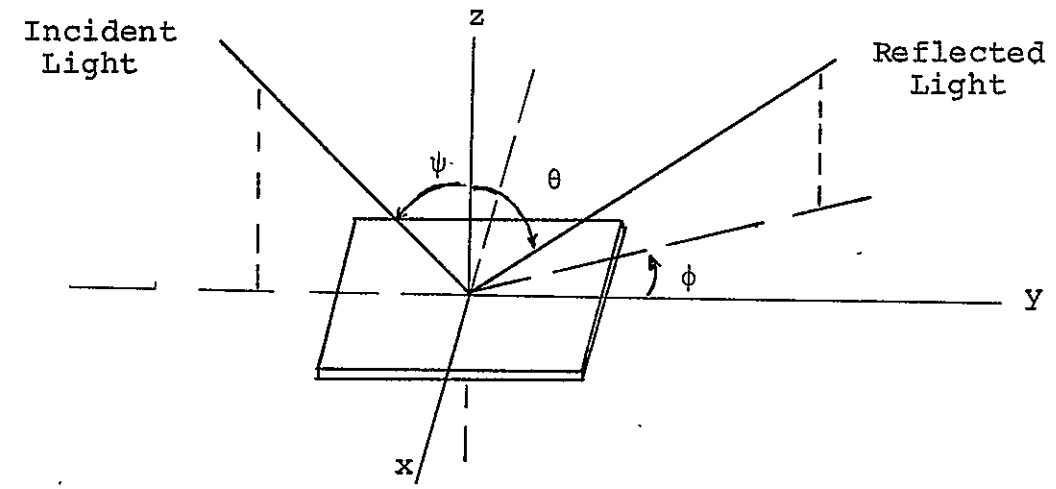

Fig. 6

The surface lies in the xy plane and the incident light is in the yz plane and makes an angle ψ with surface normal. Note that the reflected light does not reflect entirely in the yz plane. From this a relationship for the reflected light is formulated:

$$R = I\ M(\sigma_o, \varepsilon, \mu)\ \ G(\sigma, a, \lambda, \psi, \theta, \phi)$$

where R is the intensity of the reflected light (reflectance)

I is the intensity of incident light

M is a variable dependent on the material properties $(\sigma_o, \varepsilon, \mu)$

G is variable dependent on the geometrical properties

ψ, θ, ϕ are angles as given in Fig. 6.

σ, a are constants for the description of the statistical properties of the surface

λ is the wavelength of the incident light

Since the same material, copper, is used in all cases, the quantity M is a constant factor. For the first set of data, Fig. 2, the variables are the angle θ for each sample. The height variation is associated with various grades of abrasive paper. It is noted that for each test sample the resulting graph resembles a Gaussian curve but the spread is different and depends on the grain size of the abrasive paper. It is reasonable to assume that the larger grain size would produce greater surface roughness. The data confirm this assumption.

The next set of data shown in Fig. 3, has the one obvious conclusion that the polishing with the finer grain size gives the greatest reflectance. The slopes of the curves confirm this. Using the proposed general relation for reflectance, the slope is given as

$$\frac{dR}{dI} = M(\sigma_o, \varepsilon, \mu)\, G(\sigma, a, \lambda, \psi, \theta, \phi)$$

The results indicate the slope is smaller for the rougher surface. From this and the previous experiment the variation of the function is assumed to have a Gaussian form with the spread increasing with increasing surface roughness.

H. Davies considered light reflection by a rough surface with a Gaussian density function for surface variation and calculated the reflectance for two cases; a slightly rough and a very rough surface. The two results are:

Slightly rough:

$$R = I K_s \frac{a^2\sigma^2}{\lambda^4} (\cos\theta + \cos\psi)^4 \exp\{ - \frac{\pi^2 a^2}{\lambda^2} [(\sin\theta\cos\phi - \sin\psi)^2 + \sin^2\theta\sin^2\phi]\}$$

Very rough:

$$R = I\, K_v \frac{a^2}{\sigma^2} (\cos\theta + \cos\psi)^2 \exp\{-\frac{a^2}{2\sigma^2} \frac{(\sin\theta\cos\phi - \sin\psi)^2 + \sin^2\theta\sin^2\phi}{(\cos\theta + \cos\psi)^2}\}$$

where K_s and K_v are constants and a and σ are constants describing the statistical properties of the surfaces. The equations indicate the general trend of the experimental data. The various parameters are needed to relate the equations to the experimental results.

The final graph illustrates the dependence of the surface roughness on the angle of incidence. The Rayleigh criterion for surface is given by assuming light strikes a maximum and minimum height of the surface and is reflected in the same direction (see Fig. 7). The phase difference between the two paths is

$$\Delta\phi = \frac{4\pi h}{\lambda} \cos\psi$$

where h is the total height difference and ψ is the angle of incidence. If $\Delta\phi = \pi$, then cancelation occurs and no energy flows in this direction. If $\Delta\phi = 0$, it reflects specularly and is considered smooth. A value between the two extremes is more often used as indication of roughness, then for a smooth surface

$$h < \frac{\lambda}{8 \cos\psi} .$$

From the simple formulation it is obvious that as the angle ψ approaches ninety degrees moderately rough surface appears smooth. This effect is easily observed in Fig. 4. The

rougher surfaces require large incident angles before they begin to show characteristics of a smooth surface.

Appendix

Rayleigh Criterion:

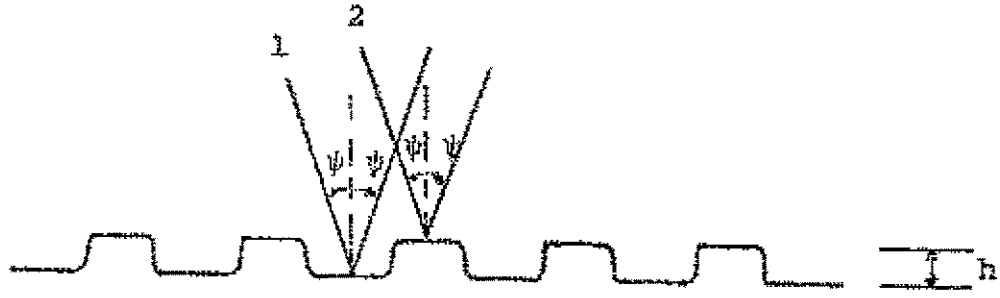

Fig. 7

Consider two rays incident on a surface with height variation of h and at an incident angle ψ. The path difference between the two rays is

$$\Delta r = 2h \cos \psi$$

and therefore the phase difference is

$$\Delta\phi = \frac{2\pi}{\lambda} \Delta r = \frac{4\pi h}{\lambda} \cos \psi$$

For small phase difference the rays are in phase and reinforce but if the phase difference is π they cancel. Since this means no energy flow in this direction, it is concluded that it has been redistributed in other directions or the surface is considered rough. Then between the two extremes is a transition region; $\Delta\phi = \pi/2$ has been chosen as well as other values as an indicator of roughness. Using this value then for a smooth surface

$$h < \frac{\lambda}{8 \cos \psi} .$$

From this a surface tends to be smooth for either $h/\lambda \to 0$ or $\psi \to 90^{\circ}$.

References

1. H. Davies, The Reflection of Electromagnetic Waves from a Rough Surface, IEE Proc., Part 4, vol. 101, pp. 209-214, 1954.

2. Petr Beckman and Andre Spizzinchino, The Scattering of Electromagnetic Waves form Rough Surfaces, Macmillan Company, New York, N. Y., 1963.

N70-36442

AN IMPROVED Q-VALUE MEASUREMENT TECHNIQUE

Introduction

In the June 15, 1969 progress report a description of a frequency measurement setup was given (1). The method was used in Q-value measurements to measure half-power frequencies and resonant frequency by observing beat frequencies with a single-frequency oscillator. The system proved to give Q-values of a resonator to a typical accuracy of ±150 parts out of 8000. A more stringent requirement was created by a surface-resistance study where the order of the maximum Q-value change was ±50. A method using a modulated oscillator for the frequency indication which gives this accuracy is described. The improvement gives Q-values of ±50 parts out of 8000. An up-to-date description of the setup is also given.

Circuitry of the General Test Bench

The bench setup as shown in Fig. 1 has a 35 GHz A-band Klystron as the signal source. Power is supplied to the A-band signal source by a Narda 62A1 power supply. The Klystron signal is fed through an isolator, an adjustable attenuator, and a 10db directional coupler. From the main guide of the coupler, the signal travels through an isolator to a precision attenuator and then into the resonator under investigation. The secondary guide of the 10db directional coupler is fed into a 3db directional coupler which serves as a power divider. The signal of the secondary arm of the 3db coupler is fed through an adjustable attenuator and a cavity-type frequency meter to a tunable detector mount. The main arm of the 3db coupler is connected to a waveguide

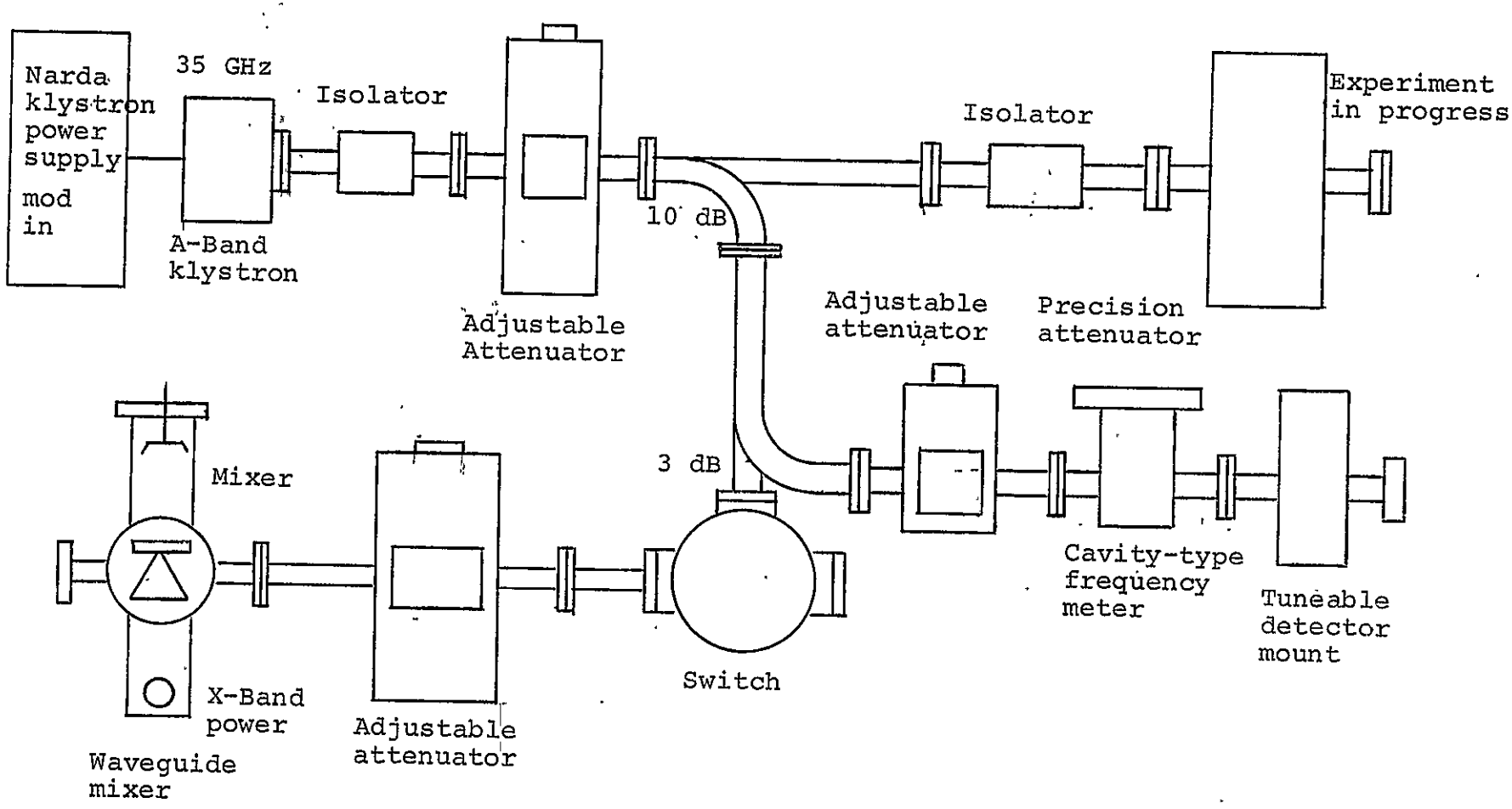

Fig. 1 Frequency measurement setup

switch. The signal from one of the switch positions is fed through an adjustable attenuator into a waveguide mixer. The other switch position may be used for other experiments (presently not in use).

Frequency Measurement

Since no frequency measurement equipment is presently available for frequencies up to 100 GHz, a special setup was developed for these measurements.

For swept frequency operation the repeller plate of the A-band klystron is modulated with a 60 Hz sawtooth waveform. This makes the klystron signal vary in frequency proportionally to the amplitude of the sawtooth voltage. The sawtooth voltage is also used as the input to the horizontal deflection plate of the HP 1200B oscilloscope. This allows the horizontal deflection of the oscilloscope to be as an approximation proportional to frequency. When the klystron signal is displayed on the oscilloscope (as a function of the repeller voltage), each position of the trace represents a frequency. In order to know the frequency which corresponds to each horizontal position of the deflected beam the heterodyne principle is being used.

A c.w. signal of known frequency (within the range of our display, which we can find by use of a cavity-type frequency meter) is mixed with the A-band signal. The A-band signal is changing linearly in frequency if we keep the amplitude of the modulating sawtooth relatively small. The known c.w. signal is the result of frequency multiplication within the mixer and originates in an x-band source that can be tuned to have its harmonic frequency within the range of that of the swept A-band

signal. The x-band signal is fed into the frequency multiplier mixer. The x-band frequency is continuously monitored on a high accuracy frequency counter.

The harmonic of the x-band signal forms a beat-frequency signal with the A-band signal. If the interference signal is superimposed on the mode pattern observed on the screen of the oscilloscope, a zero beat pattern can be seen. This pattern actually is a sine wave with a frequence equal to the difference between the instantaneous A-band frequency which is swept linearly by the sawtooth and the harmonic of the x-band signal frequency. A zero beat occurs at a specific position of the beam when the known harmonic of the x-band signal is equal to the unknown A-band signal. By this, the horizontal deflection of the oscilloscope (sweep proportional to the frequency of the A-band signal) can be calibrated in terms of the frequency with counter accuracy.

Circuitry for Frequency Measurements

A Model 540A function generator by Exact Electronics is used for generation of a sawtooth wave with a frequency of approximatel 60 Hz. This signal is applied to the horizontal input of the HP 1200B oscilloscope, and also to the external modulation jack of the 62A1 klystron power supply for the A-band klystron. This makes the frequency of the signal of the A-band varying in the form of a sawtooth linearly with time. To keep the operation linear the sawtooth has to be relatively small. By applying this same waveform to the horizontal deflection plates of the oscilloscope, the display is then a function of frequency. On channel B of the oscilloscope the mode pattern of the A-band klystron can be monitored. With a cavity-type frequency meter the approximate

center frequency of the klystron mode can be found. This approximate frequency divided by the number of a convenient harmonic yields the frequency of the x-band source.

The c.w. x-band signal is generated by a Varian X-13 x-band klystron and is fed into a Demornay Bonardi DBGD-350 crystal multiplier-mixer. The frequency of the x-band source is monitored by a HP 5245A frequency counter. The other input signal to the crystal mixer is the sawtooth-modulated A-band signal. Variable shorts on the crystal mixer permit adjustments for optimum frequency multiplication and mixing. The crystal current is not to exceed 50 μa.

The output signal of the crystal mixer is amplified in an AC amplifier (10Hz to 1.5 MHz) and fed into an RC-filter. The output is capacitively coupled to the line connecting the crystal detector for monitoring the klystron mode to channel B of the oscilloscope. On the screen of the oscilloscope, the mode pattern is then displayed with the interference signal superimposed on it. The control knob for the reflector voltage on the X-13 signal source power supply (HP 716B Klystron Power Supply) can be used to bring the two frequencies closer together. The zero beat between the two spikes of the interference pattern corresponds to the condition that both frequencies are equal. The x-band source is constantly being monitored by the accurate HP 5245A frequency counter. Multiplication of the monitored frequency by the number of the harmonic gives the unknown frequency at the horizontal position of the beam indicated by the zero beat.

The measurement of a segment of the scope trace corresponds to a difference in frequency. If the x-band source reflector

voltage is modulated (HP Signal Generator 606A)*. The indication on the scope has the form as shown in Fig. 2b . Because we are using the fourth harmonic, one fourth of the frequency of the modulating signal is the difference frequency on the scope of the first sideband from the carrier. The beat-frequency spectrum displayed on the oscilloscope is used to measure the half-power frequencies of the resonance curve.

Q-Value Measurements

The resonator to be measured is inserted into the experimental branch of the general setup. The signal from the A-band klystron is coupled into the resonator and the output resonance curve is displayed on channel B of the Hp 1200 B oscilloscope. On channel A the mode pattern of the klystron is displayed. By adjusting the positioning of the traces and the attenuation of the signals, one signal is placed on the top of the other so that the peak of resonant curve touches the klystron mode curve. (see fig. 2a). The resonant curve is increased by removing 3db of attenuation making the intersection of the two curves be at the half-power points of the resonant curve. Than taking the beat-frequency spectrum of the indicator when the reflector voltage of the x-band klystron is modulated and aligning the first sidebands with the intersections, the half-power frequency difference is found. We now have a display that appears like that in Fig. 2b . Since the carrier frequency as displayed

*The x-band signal consists of the carrier and side-frequencies ΔF apart, where ΔF is the modulation frequency.

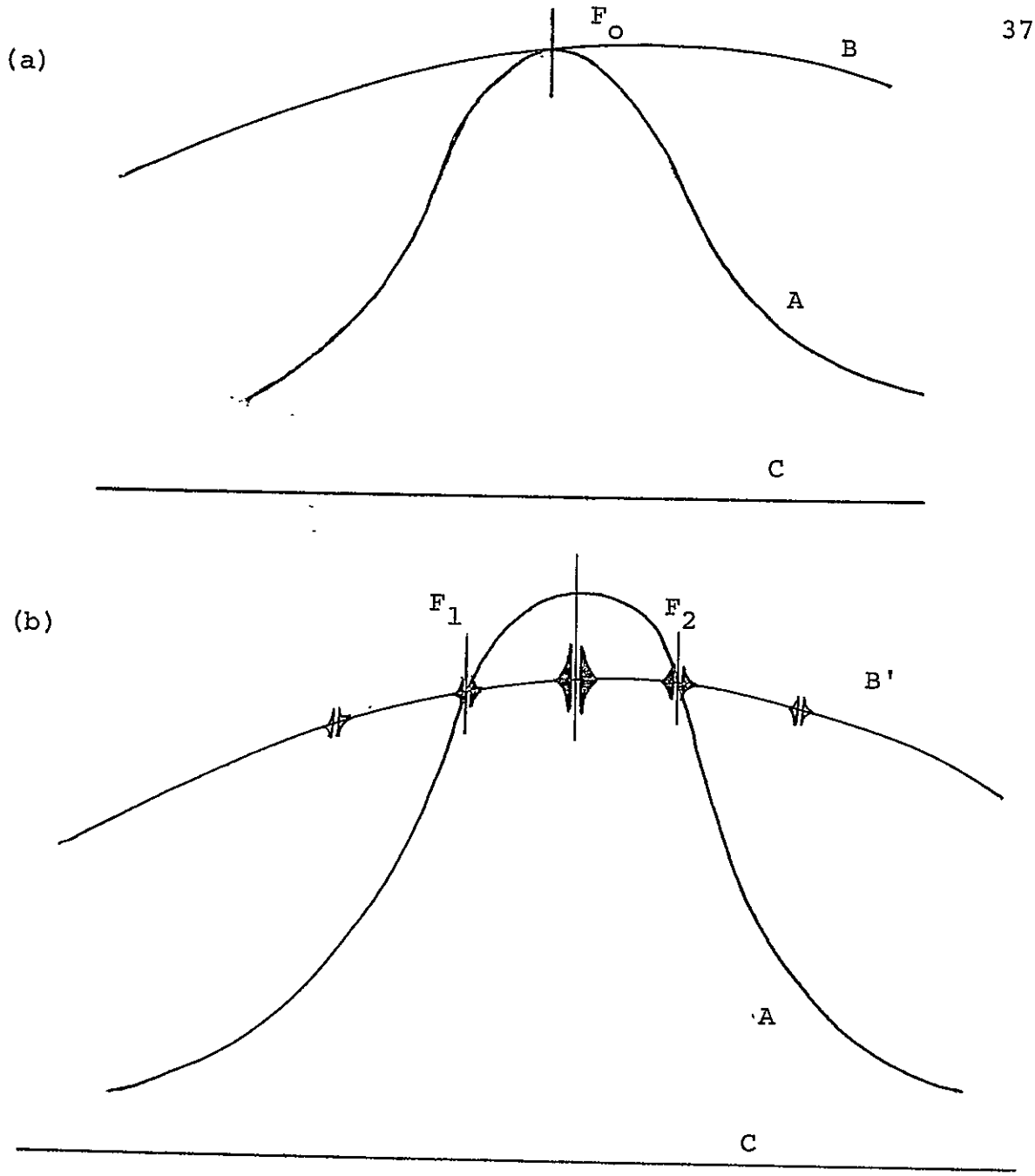

Fig. 2 Dual beam displays on oscilloscope for a Q-value measurement.

(a) Initial setting.

(b) Resonance input increased by 3 dB.

A. Cavity resonance curve.

B. Klystron-mode curve.

B'. Klystron-mode curve with superimposed interference pattern.

C. Zero level.

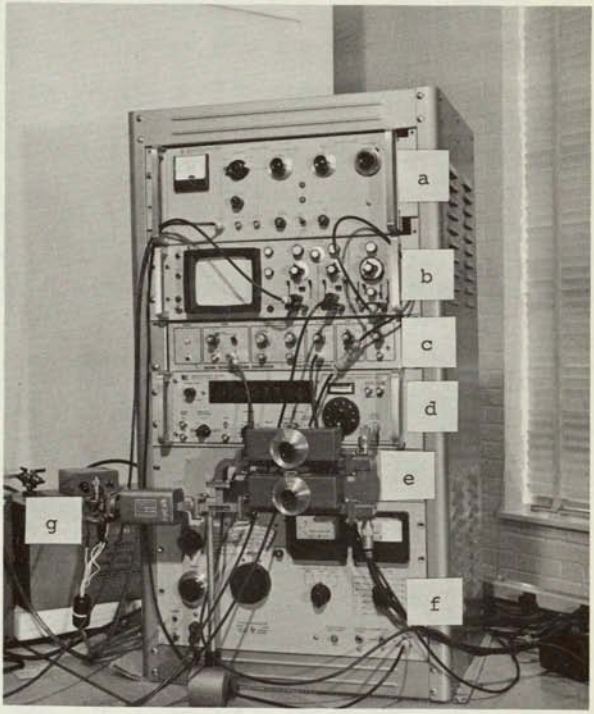

Fig. 3 Monitor console for frequency measurement setup
a X-band power supply
b Dual trace oscilloscope
c Function generator (sawtooth wave)
d Frequency counter
e Microwave circuitry
f Modulation signal source
g X-band Klystron

on the oscilloscope is that of the x-band source, the correct frequency (because we use the fourth harmonic) is four times that of the x-band signal. The first sideband frequency must be doubled to get the total frequency difference (note that the first sideband frequency display on the scope is one-fourth the frequency of the modulating signal). With points F_1 and F_2 corresponding to the half-power frequencies, the loaded Q is $F_o/(F_2-F_1)$.

References

1. R. A. Kraft and F. J. Tischer: Frequency Measurement Setup for Millimeter Waves, Progress Report - Grant NGR 34-002-047/52, pp 28-38 (June 15, 1969).

N70-36443

CHARACTERISTICS OF DENSE WIRE GRIDS

Abstract

As a supplement to preceding considerations, this report deals with the characteristics of wire grids with narrowly spaced wires. The presently used equations are reviewed from the viewpoint of their application at decreasing spacing between the wires. Modified equations are developed for lossless and lossy grids for the region of spacing between zero and values where customary equations can be applied.

Introduction

In preceding reports[1,2] the characteristics of wire grids were considered to find relationships to be used for the study and the design of the fence guide. At the derivations, equations were used from a few major articles [3,4,5,6] and the results compared with those obtained by experiments. Satisfactory agreement was obtained. At the continued study of the fence guide, less spacing between the wires of the grids was applied recently. This had the consequence that the known equations are no longer applicable and that a modification of the previously used relationships became necessary to allow computations in the region of decreasing spacing. Derivation of the modified equations and the resulting relationships for lossless and lossy wire grids are presented in this report.

Review of Relationships

Two basic relationships derived by various authors are known and can be used for the computation of the surface impedance of

wire grids. One of these was derived directly for grids with round wires and has the following form

$$Z_p = j Z_o \frac{s}{\lambda} \ln \frac{s}{\pi d} \cdot \qquad (1)$$

The other equation represents a modified relationship derived originally for grids composed of strips. At the modification, the surface of the circular conductors was assumed to equal that of the strips. The resulting equation is

$$Z_p = j Z_o \frac{s}{\lambda} \ln \csc \frac{\pi d}{s} \cdot \qquad (2)$$

We observe that substituting the argument $1/(\pi d/s)$ for the cosecant, which is valid for large spacings, makes the two equations become identical. Since in the present case the spacing and the wire diameter usually are much smaller than the wavelength, a correction factor, originally introduced by MacFarlane[3], is disregarded.

Considering the application of these equations to the fence guide, it was found that the second equation gives a larger range since it can be used for smaller spacing than Eq. (1). The latter [Eq. (1)] gives a negative impedance if the term $s/\pi d$ becomes smaller than unity. It was also found that Eq. (2) gives better agreement with the experimental results.[2]

The equations can be rewritten in somewhat different form by combining the geometry parameters to form separate terms We

write hence

$$Z_p/Z_o = j\left(\frac{d}{\lambda}\right)\left(\frac{s}{d}\ln\frac{s}{\pi d}\right), \tag{3a}$$

$$Z_p/Z_o = j\left(\frac{d}{\lambda}\right)\left(\frac{s}{d}\ln\csc\frac{\pi d}{s}\right). \tag{3b}$$

It becomes advantageous to substitute for the geometry term s/d a new variable t = s/d - 1. This variable actually indicates the width of the gap between the wires normalized with regard to the wire diameter d. The new variable becomes zero when s/d approaches one and the wires touch each other.

It is interesting to inspect plots of the second factors of Eqs. (3) which are shown in Fig. 1 as functions of t. Curve A represents the second factor of Eq. (3a) and B the corresponding term of Eq. (3b). The graph also contains the values of this factor obtained by the evaluation of measurements of the surface impedance in the X-Band regions described in previous reports.[2] They are indicated by D and E. We observe that the two curves A and B approach the abscissa at finite values of t. This indicates that the corresponding relationships are incorrect for small spacing and not valid since the impedance cannot approach the value zero while a gap exists between the wires. A modification of the relationships is hence necessary to satisfy the condition that the impedance approaches gradually and monotonously zero for t = 0.

As the next step, an empirical method is chosen to find an approximate relationship to represent the second factor in the equation for the wire grid impedance in terms of t for small

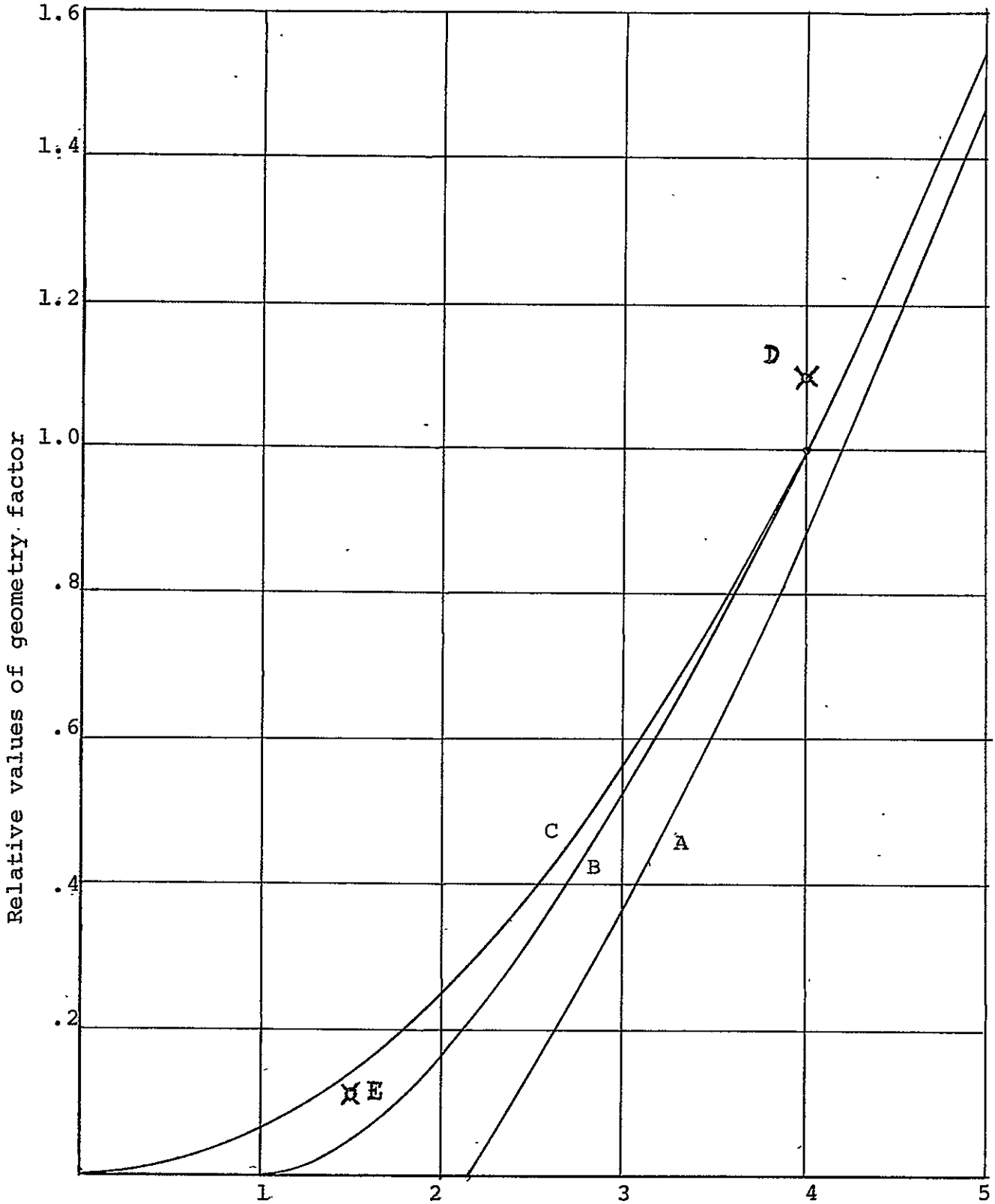

Fig. 1. Geometry factors for dense wire grids.
A. $(s/d)\ln(s/\pi d)$.
B. $(s/d)\ln \csc(\pi d/s)$.
C. $(s/d - 1)^2/4$; $t < 4$.

values of this quantity. The conditions for the choice of a useful relationship are the following: The relationship should be simple, it should give zero for p = 0 and should gradually become Eq. (2) for increasing values of p. A relationship based on t^a was chosen to accomplish this. The relationship is shown graphically as curve C in Fig. 1 with a = 2 as a satisfactory choice. It is given mathematically by

$$\frac{\left(\frac{s}{d}-1\right)^a}{4^a} = \frac{\left(\frac{s}{d}-1\right)^2}{4^2} .$$

We observe that the quadratic relationship valid for s/d < 5 (t < 4) assumes the value of the second factor in Eq. (3b) for s/d = 5 or t = 4. The measured value indicated by E is now very close to the theoretical value obtained by the new relationship. Since the value of the second factor of Eq. (3b) is 2.67 for t = 4 (s/d = 5), the new approximate equation for the impedance for small spacing becomes

$$Z_p/Z_o = j\left(\frac{d}{\lambda}\right) 0.167\, t^2 = j\left(\frac{d}{\lambda}\right) 0.167 \left(\frac{s}{d}-1\right)^2. \quad (4)$$

Effect of Conduction Losses.

It can be assumed that the customary relationships for taking into consideration the losses on the wires are no longer valid at small spacing. These relationships take into account the losses by assuming that the current along each wire is uniformly distributed around the wire and by adding to the surface

impedance of the grid a term[5]

$$R_s \frac{s}{\pi d}(1+j) , \qquad (4a)$$

where R_s is the surface resistance of the grid material.

There are two aspects which have to be taken into consideration for small spacing. First, the distribution in circumferential direction of the current along the wires is no longer uniform and is such that the major part of the current flows on the input half of the circumference. This is the case since, due to the considerable reflections by the dense grid, the fields and the surface current are low on the output side. Hence, only one-half of the circumference πd [in the denominator of Eq. (4a)] is practically available to carry the grid current. Furthermore, the current will not be uniformly distributed on the input half of the circumference of the grid wires. It will be a maximum in the center where the magnetic field lines are dense and low on the sides of the cylindrical wires where the surfaces of adjacent wires face each other. The local contributions to the losses by the parts of the surfaces on the sides will be very small, since these contributions are proportional to the square of the relative local surface currents and local magnetic fields. A satisfactory approximation is offered by assuming a sinusoidal distribution of the current around the input half of the wire circumference. This allows simple determination of the maximum current density in the center. The integration of the current over the input half of the circumference gives the total current per wire

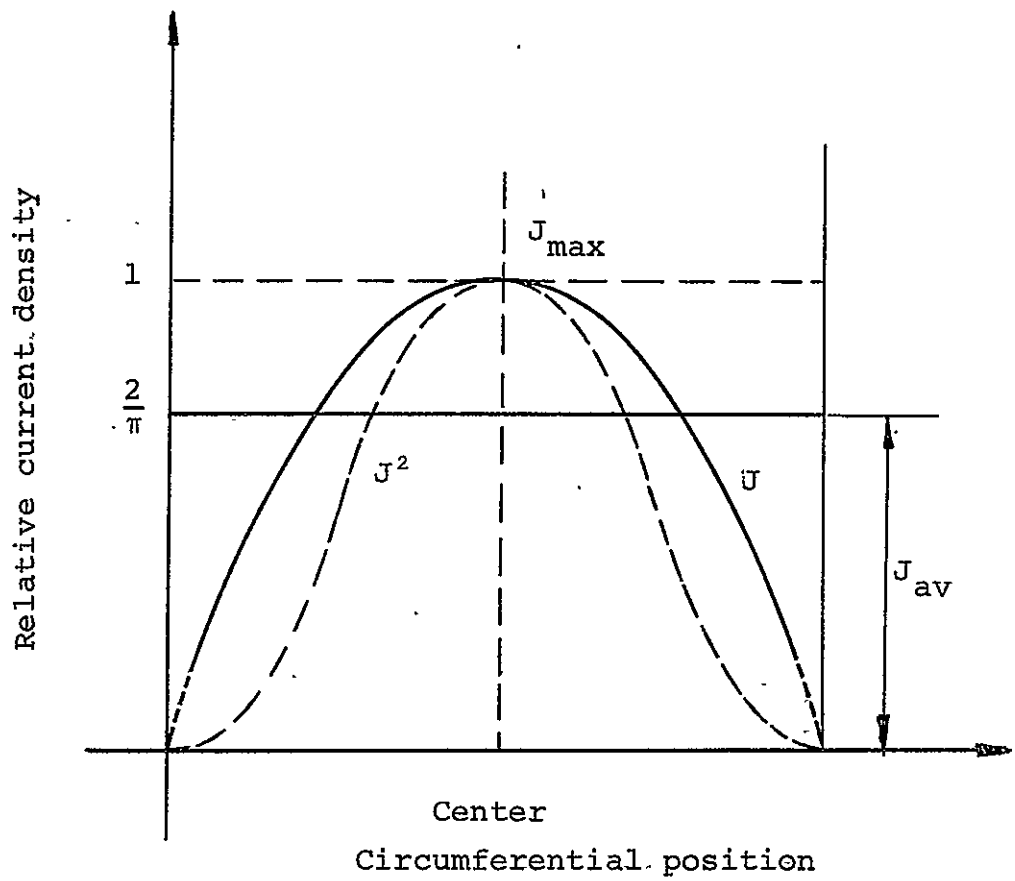

Fig. 2 Circumferential distribution of longitudinal current on wires.

resulting from the incident waves. We can write

$$J_{max} = J_{av} \frac{\pi}{2}, \tag{5}$$

since the average value of a sine wave is $2/\pi$. Based on this current distribution, we can subsequently determing an equivalent surface resistance R_s' according to

$$J_{av}^2 R_s' \pi \frac{d}{2} = \int_0^{\pi \frac{d}{2}} J^2(x) R_s \, dx ,$$

where the distribution of $J^2(x)$ is given by the dotted line in Fig. (2). Evaluation of the integral yields

$$J_{av}^2 R_s' \pi \frac{d}{2} = J_{max}^2 \frac{1}{2} \pi \frac{d}{2} = \left(\frac{\pi}{2}\right)^2 J_{av}^2 \frac{\pi d}{4} .$$

It follows

$$R_s' = \frac{\pi^2}{8} R_s = 1.23 \, R_s . \tag{6}$$

Taking into consideration that only one-half of the circumference of the wire is available to carry this current, we find for the contribution to the impedance of the wire grid

$$Z_{w\sigma} = \frac{sR_s'}{\pi d/2}(1+j) = 2.46 \frac{sR_s}{\pi d}(1+j) . \tag{7}$$

This indicates that for a closed wire grid the effect of the losses increases by about a factor 2.46 in comparison with wide grids.

The variation of the constant 2.46 with increasing spacing can be taken into account by substituting for it a term which linearly decreases with increasing t. The assumption is made that, for a spacing given by t = 4, the constant has decreased to

a value 1 giving the equation the customary form expressed by Eq. (4a). The relationship which satisfies these conditions is given by

$$2{,}46 - 0.365\,t$$

It follows that the approximate equation for the contribution of the conduction losses to the surface impedance has the form

$$Z_{w\sigma} \approx (2.46 - 0.365\,t)\,\frac{s\,R_s}{\pi d}(1-j)\,. \qquad (8)$$

The equation is valid in the region $0 < p < 4$ $(1 < s/d < 5)$.

The total approximate surface impedance of the wire grid in this region is hence

$$Z_w = j\,0.167\,Z_0\,\frac{d}{\lambda}\left(\frac{s}{d}-1\right)^2 + (2.46-0.365t)\,\frac{s\,R_s}{\pi d}(1+j)\,. \qquad (9)$$

The derived relationship will be used until more exact equations will become available. It can be expected, however, that more accurate equations will not drastically change the relationships.

References

1. Progress Report on "Study of Rectangular-Guide-Like Structures for Millimeter-Wave Transmission", October 15, 1968, pp. 4-42.

2. Progress Report on "Study of Rectangular-Guide-Like Structures for Millimeter-Wave Transmission", February 15, 1969, pp. 28-39.

3. G. G. MacFarlane, Surface Impedance of an Infinite Parallel-Wire Grid at Oblique Angles of Incidence, J. Inst. Elec. Engrs., pt3A, vol. 93, p1523-1527; 1946.

4. N. Marcuvitz. Waveguide Handbook, p280-284, M. I. T. Radiation Laboratory Series 10, McGraw-Hill, New York.

5. J. R. Wait, Effective Impedance of a Wire Grid Parallel to the Earth Surface, IRE Trans. on Ant. and Prop., vol. AP-10, p538-542, September 1962.

6. E. A. Lewis and J. Casey, Electromagnetic Reflection and Transmission by Gratings of Resistive Wires, J. Appl. Phys., vol. 23, p605-608; June, 1952.

N70-36444

FENCE GUIDE MEASUREMENTS

Abstract

Measurements of the field distribution in 175 mm long fence guide sections are discussed and an evaluation of the parameters is made.

In the previous progress report (NGL 34-002-047 of February 15, 1970) electromagnetic field measurements were carried out at 35 GHz on a fence guide model 47.5 mm long. The measurement setup was also included. At present measurements are carried out on a longer section of fence guide.

Two 175 mm long fence guide sections were fabricated using copper wires of diameter d_w = 0.862 mm, spacings s_w = 1.17 mm and 1.016 mm on a dielectric sheet with a thickness 2d = 0.80 mm and ε_r = 2.53 (Rexolite). The prototype sections are shown in Fig. 1. The measurements were made at 35.0 GHz and an improved capacitive monopole with compensation was used as a field probe. A thin copper sheet was used as a short in some cases of the measurements and the output response was recorded with the help of an X-Y recorder.

The VSWR pattern with load end shorted (Fig. 2) was measured over the full 175 mm length of the fence guide. The minima over the entire length were precisely located and a mean separation of 5.442 mm found. The guide wavelength for the fence guide at 35 GHz computed from the average distance between the minima is λ_g = 10.884 mm.

The field decay was measured in the x-direction away from the dielectric, with the fence guide short circuited, at the locations of first, second and the fourth maximum and up to the height of the fence wires. The exponential decay of the electric field was plotted on a linearized db scale (Fig. 3). If averaging technique is used, the lines are straight and fairly parallel to

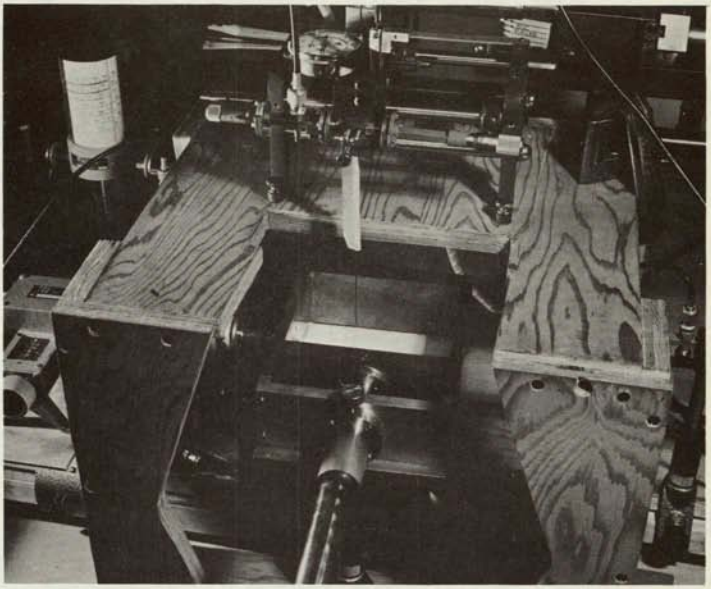

Fig. 1 Measurement setup for the study of an open cylindrical-reflector resonator.

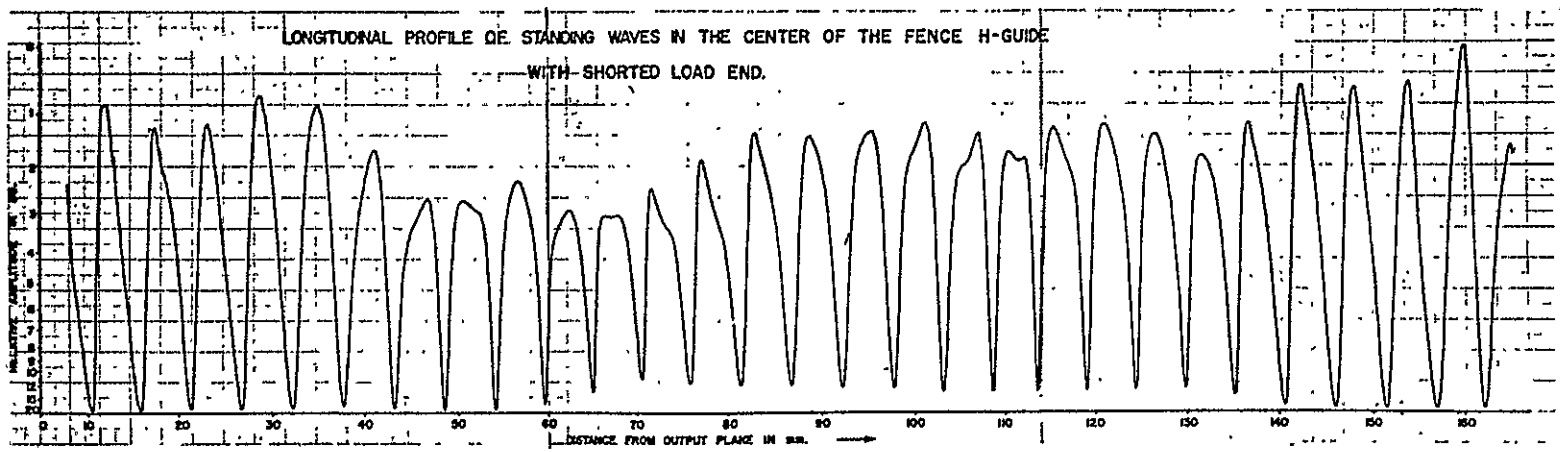

Fig. 2 Standing-wave pattern on a fence guide section

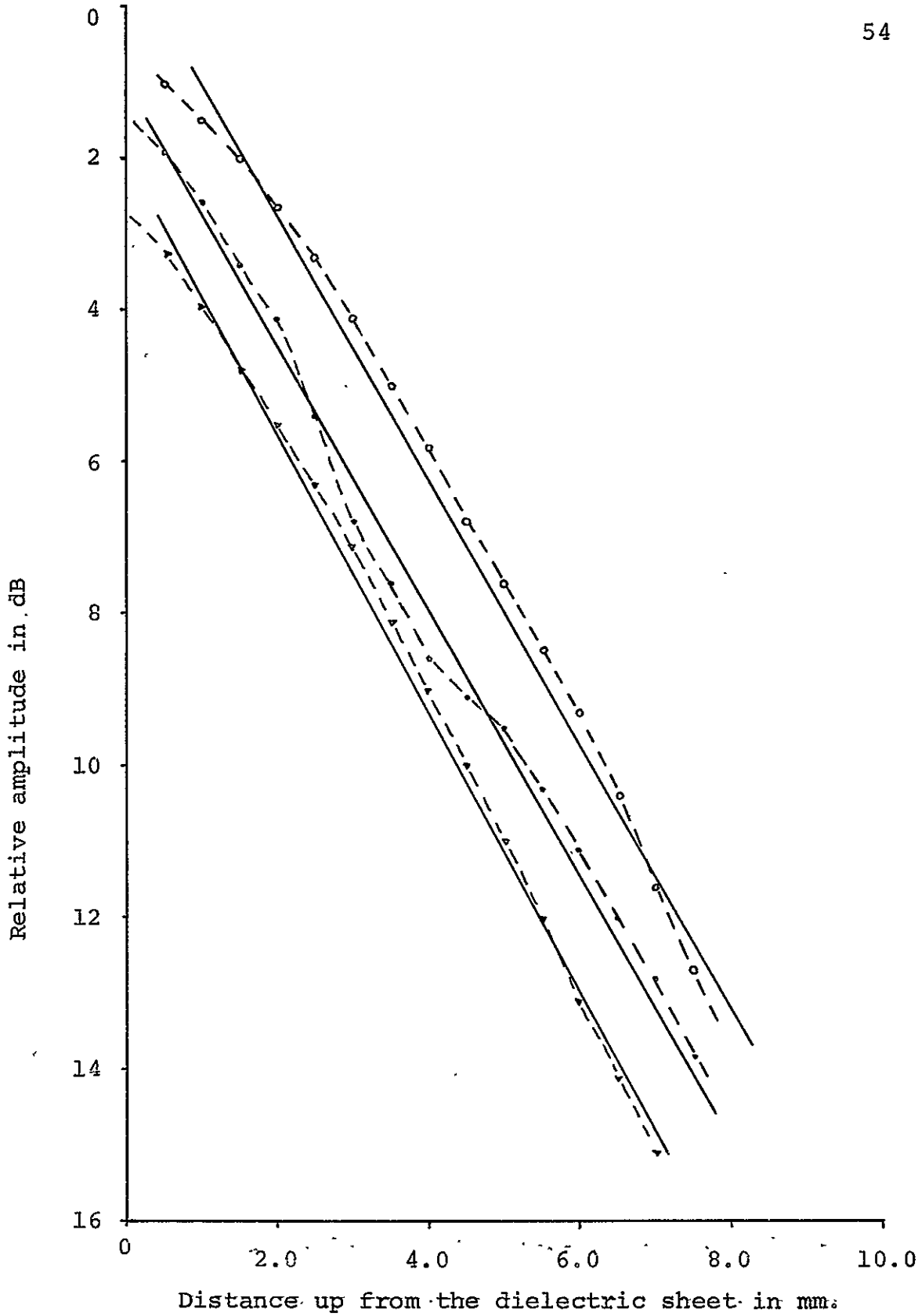

Fig. 3 Exponential decrease of field strength inside the fence guide

each other. The slope of the lines gives the exponential decay factor α_x varying somewhere in the range of 1.67 dB/mm to 1.80 dB/mm. The corresponding decay factor as measured on the Standard H-guide has an average value of 1.53 dB/mm.

Field measurements were made to compare the level of the field strength inside (Fig. 4) at the center and outside (about 3 mm away from the fence) with a short circuited load. The field strength is indicative of the leakage of field through the wires of the fence. The maximum field measured outside was at least 36 dB below the maximum field inside.

The variation of the x-component of the electric field in the transverse direction was measured at the location of the first three maxima from the short circuit for various heights above the dielectric sheet (Fig. 5). The variation has a sine form as was expected. It showed some irregularity in the form for the third half-period.

Figure 6 shows the field distribution measured in transverse direction at the level of the upper edge of the fence wires. The parameter is the distance above the upper edge.

In an effort to obtain some idea of the attenuation in the longitudinal direction, VSWR measurements were carried out using a tunable matched load. The pattern obtained had a reasonable trend for the envelope and, the attenuation was preliminarily computed at a standing-wave ratio 1.05 for the load. The value so obtained was .066 dB/mm. The measurements are being continued.

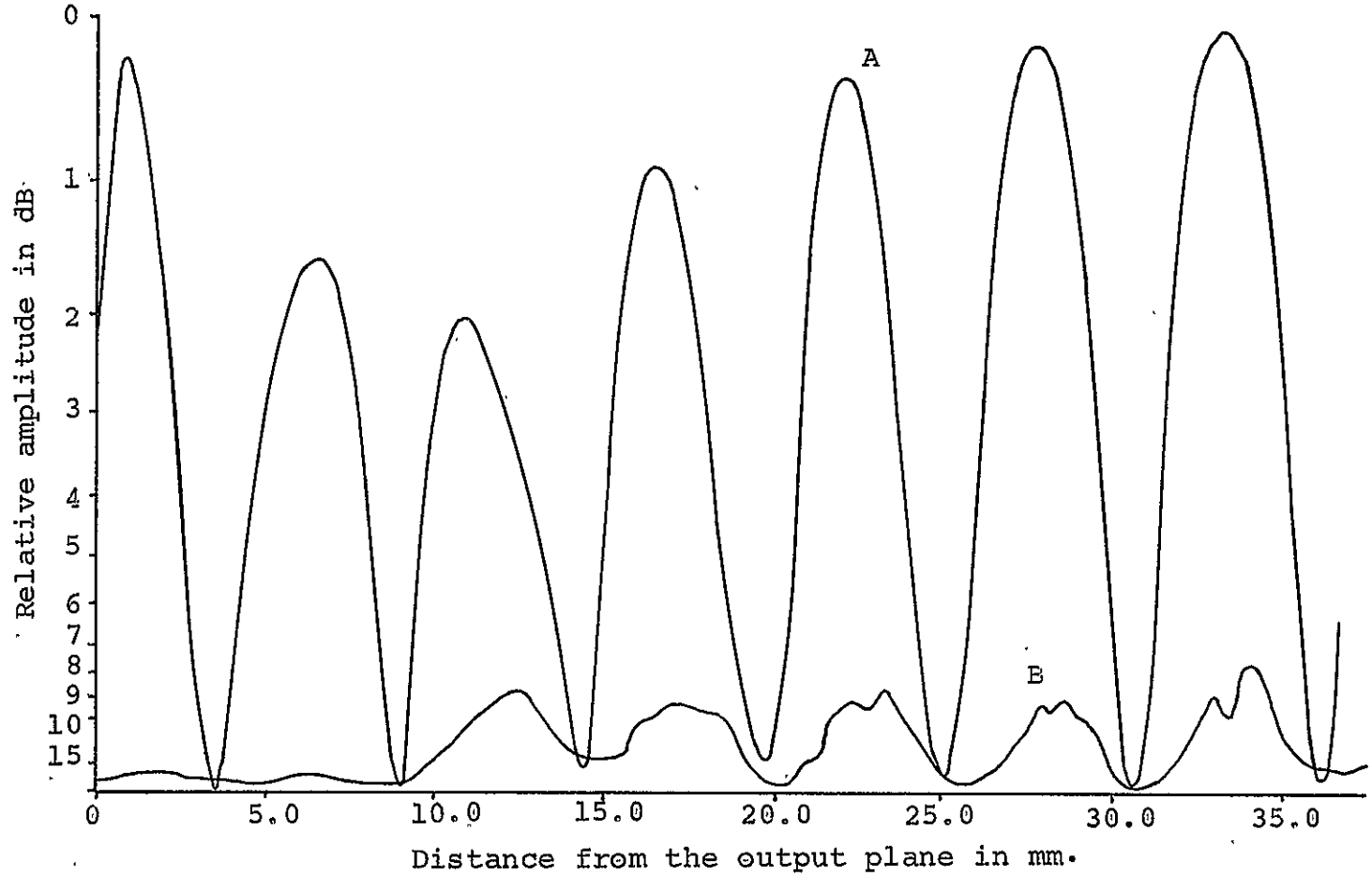

Fig. 4. Longitudinal field distribution
A. Inside in center of the guide.
B. Outside the guide (increased by 30 dB).

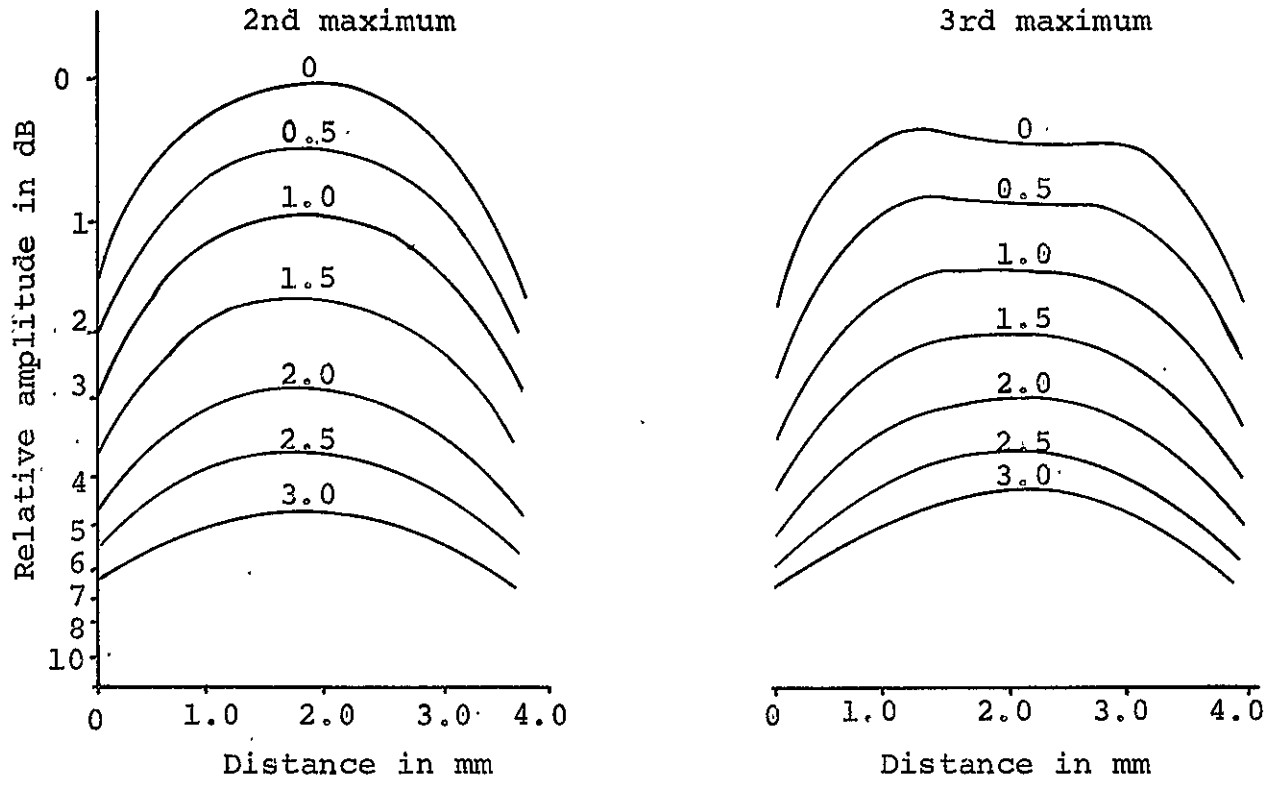

Fig. 5. Field distribution inside the guide at various levels of height.

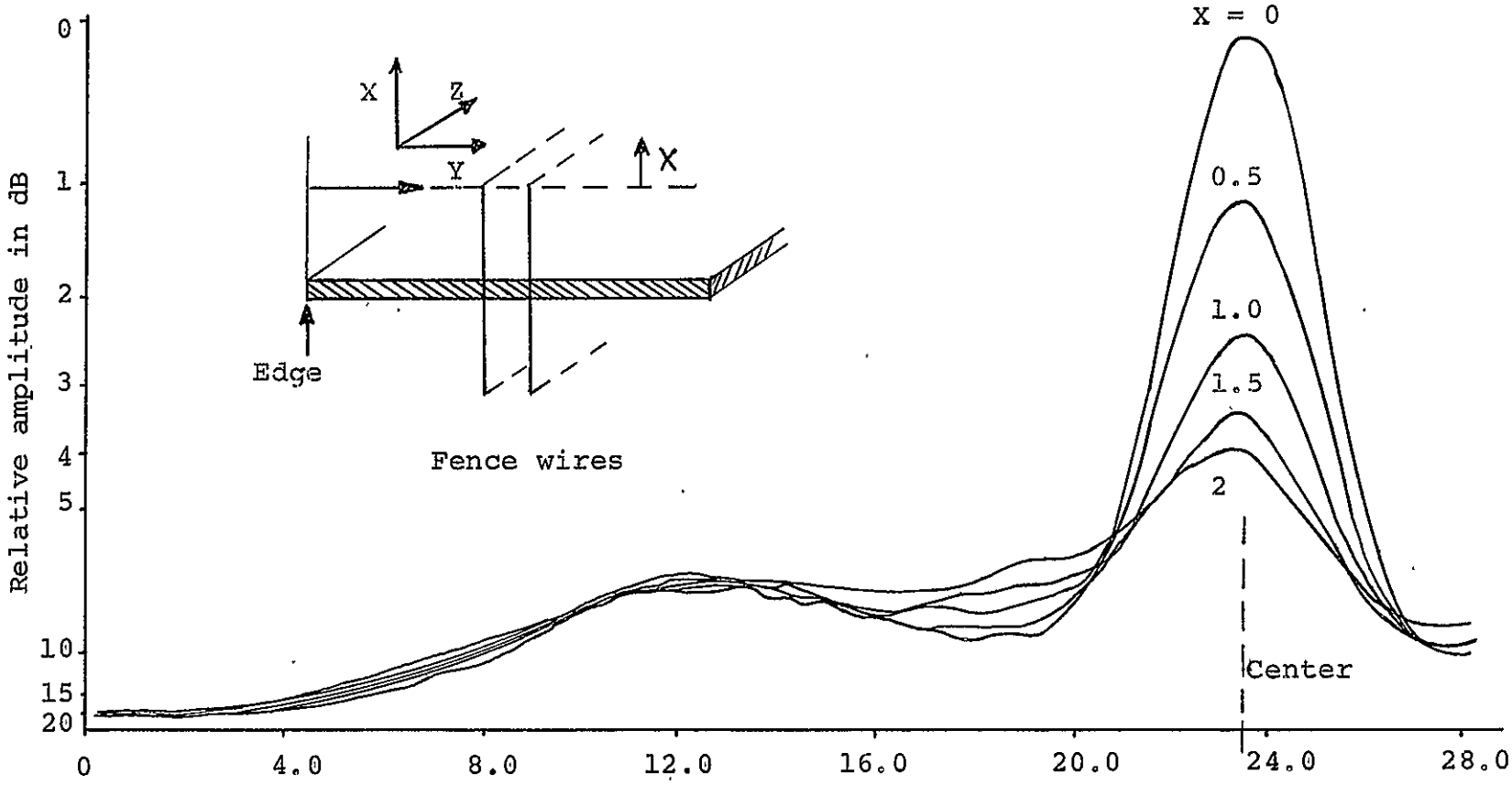

Distance from the dielectric sheet edge in mm.

Fig. 6 Transverse field distribution above fence guide.

N70-36445

STUDY OF OPEN RESONATORS WITH CYLINDRICAL REFLECTORS

Abstract

An experimental investigation of a non-confocal open resonator with cylindrical reflectors is reported. The resonator was operated at 36.8GHz. Measurements were made of the Q-value and of the field distributions as a function of reflector spacing. Mode numbers were obtained from these plots and an attempt was made to find relationships between the mode numbers m,n,p, the spacing 'b' between the reflectors, and the Q-value.

Introduction

In several papers[1,2] related to the study of open resonators for millimeter waves, confocal systems (distance of separation between the reflectors equal to the radius of curvature of the reflectors) which are considered optimum from the point of view of diffraction losses were investigated. The possibilities of instabilities of this system were reported.[3,4]

Investigations made in this laboratory on two confocal resonators with cylindrical reflectors manufactured to normal machining tolerances gave unsatisfactory operation and relatively low Q-values. However, regions of considerably higher 'Q' of the order of 30,000 were observed with the same reflectors for reduced distance between the reflectors ($r/2 < b < r$). Based on these results it can be concluded that deviations from confocal geometry may be preferable. The tolerances at the fabrication

of the two reflectors and also the uniformity of spacing between them may not have to be as rigid as required for the confocal case. A detailed study of the properties of non-confocal systems is in progress.

Experimental Study

The main purpose of the present investigation is to study the properties of the open resonators with cylindrical reflectors over a wide range of spacing between them and to find out whether there exists any relationship between the Q-value, the geometry parameters, and the mode numbers. Field distributions are measured inside the cavity at resonance, the mode numbers determined, and the Q-values found. The setup used for the investigations is shown in Fig. 1. The geometry of the cavity is indicated in Fig. 2.

Results

The distance of separation was varied within the range $0.5 < r/b < 1$. A manual system was used to move one of the reflectors with respect to the other in such a way that the apertures of the reflectors remained parallel and their symmetry planes coincide. In two ranges the observed Q-values were of order of 30,000. The distance between the reflectors in these two ranges were

1. $b \simeq r/2 + 0.5$ cm
2. $b \simeq r - 0.5$ cm

A considerable mode interaction and irregular resonance patterns were observed for other spacings. The resonance pattern of some

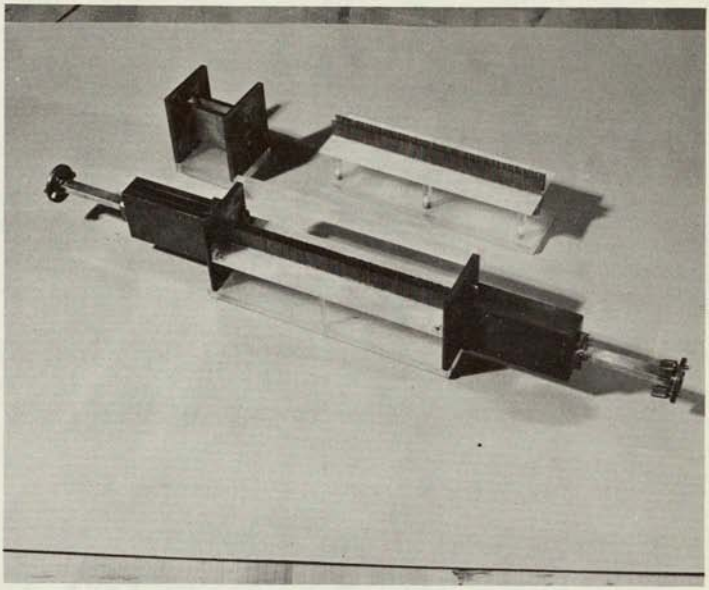

Fig. 1 Prototype sections (L = 175 mm) of fence guide

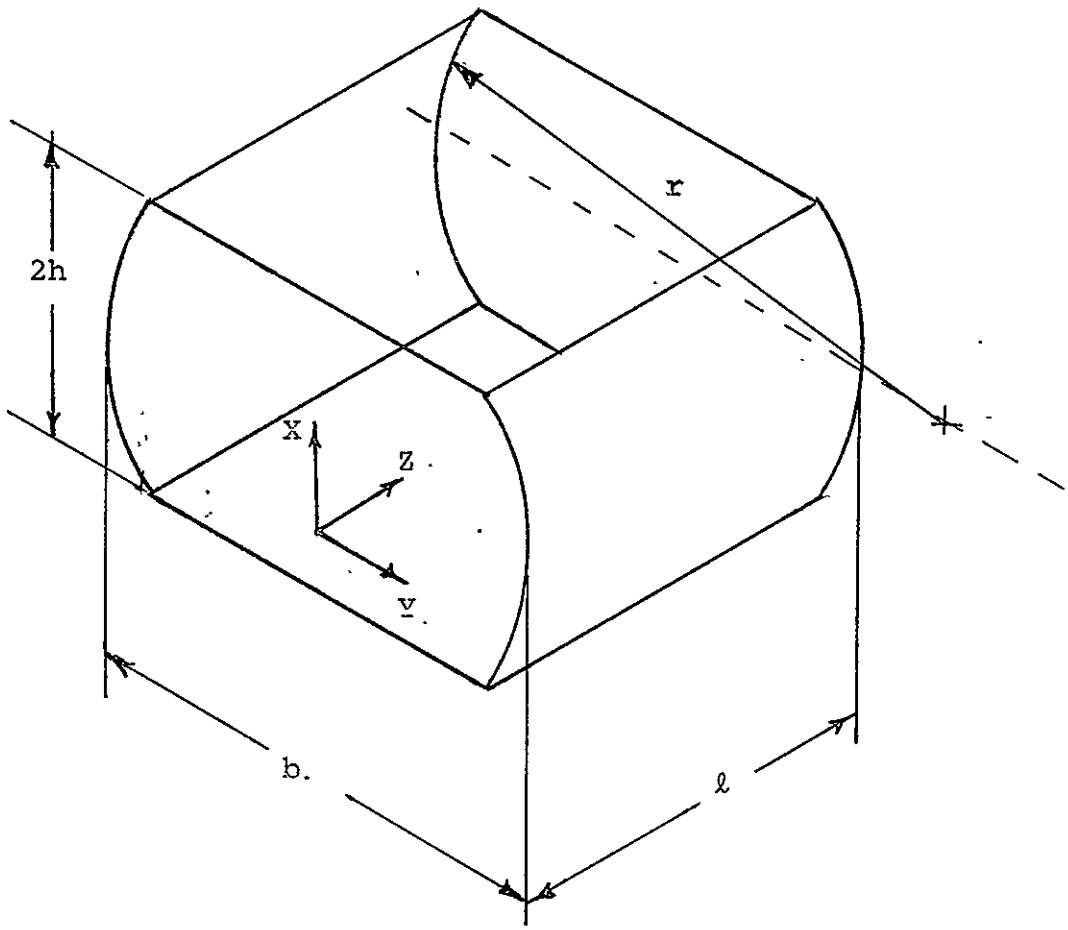

X, Y, Z: Rectangular Coordinates Axes

m: Mode number along 'x' axis

n: Mode number along 'y' axis

p: Mode number along 'z' axis

Q: Quality factor

b: Spacing between reflectors

r: Radius of curvature of the reflectors

Fig. 2. Geometry of resonator

of the high 'Q' modes were not symmetric, and no correlation between the Q-values and spacing was found.

Measurement of Field Distributions.

The aperture distribution as well as the transverse distribution were obtained by moving a compensated probe inside the cavity and using the output of the probe to drive a plotter. The plots are shown in Figures 3 and 4 for various values of 'b'. From Fig. 3 it is verified that the aperture distribution across the reflector is approximately Gaussian. The field at the rim is about 12 db below that in the center. An example of the transverse field distribution is shown in Fig. 4. The mode numbers were obtained by evaluation of the transverse field distributions. No correlation seems to exist between the mode number n and the Q-value. The only conclusion that one can draw at this time is that the Q-value decreases with increasing p. Further studies with modifications of the coupling elements between the resonator and the waveguide coupling energy in and out are in progress.

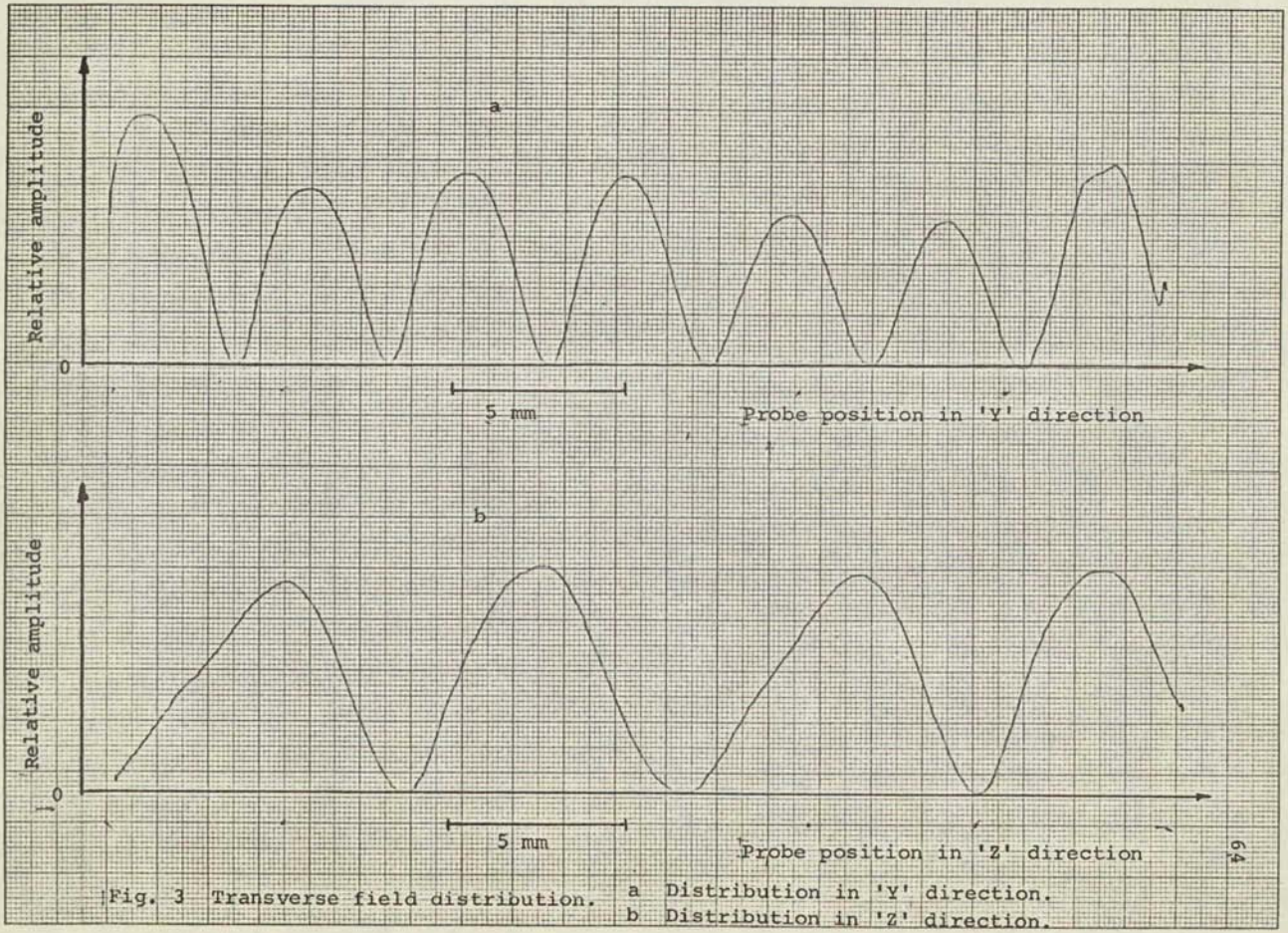

Fig. 3 Transverse field distribution. a Distribution in 'Y' direction. b Distribution in 'Z' direction.

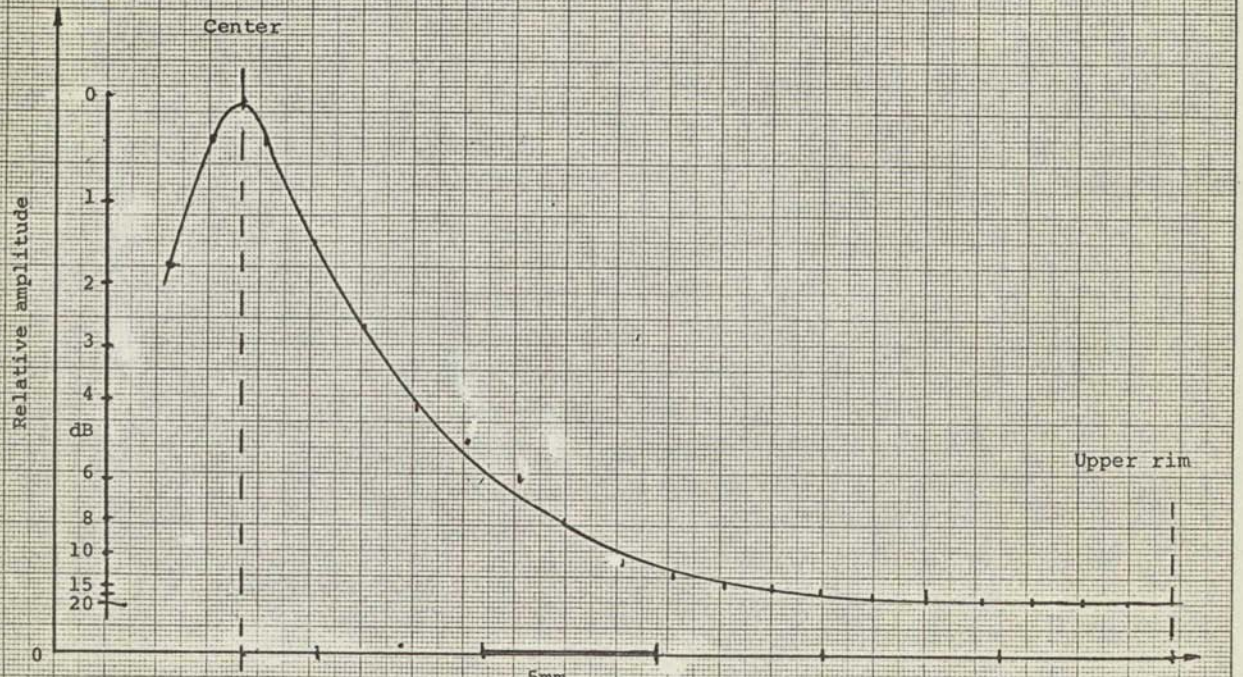

Fig. 4 Vertical field distribution (aperture distribution).

References

1. G. D. Boyd and J. P. Gordon, "Confocal Multimode Resonators for Millimeter through Optical Wavelength Masers," Bell System Tech. J., vol. 41, pp. 489-589; March, 1961.

2. L. A. Vainshtein, "Open Resonators for Lasers", JETP (USSR), vol. 44, pp. 1050-1067, March, 1963.

3. R. W. Zimmerer, "Spherical Mirror Fabry-Perot Resonators", IEEE Trans. on Microwave Theory and Technique," vol. MTT-11, pp. 371-379, Sept., 1963.

4. G. D. Boyd and H. Kogelnik, "Generalized Confocal Resonator Theory," Bell System Tech. Journal, vol. 41, pp. 1347-1369, July, 1962.

N70-36446

OPEN-WAVEGUIDE CHARACTERISTICS BY FIELD MATCHING

Abstract

Field matching method is used for considering a parallel-wall waveguide. Herewith the cross-section is subdivided into regions, those between the center conductor and the sidewalls and those adjacent to the former. The potential equations derived for the various regions contain two sets of unknown coefficients. To determine these coefficients, potential and E-field are matched at the boundary surfaces between the regions. The resultant set of infinite simultaneous equations is solved on the computer using a 20-term approximation. The potential distributions in x and y directions along two lines are plotted and compared with the result of a numerical solution. The line impedance is obtained for several sizes of the center conductor and a plot is given.

Introduction

In this report, the field matching method of solving electromagnetic field and wave propagation problems in parralel-wall waveguides is analyzed. It is studied in relation to a rectangular conductor between the walls. The results are compared with the solution of the static electric potential problem using a simple numerical technique.

Field Representation

Consider the parallel wall waveguide with the inner conductor shown in Figure 1. For TEM operation, Laplace's equation is obtained which is applied in the two regions I and II:

$$\nabla^2 \phi_1 = 0 \qquad x \geq d \;,\; 0 \leq y \leq a$$

$$\nabla^2 \phi_2 = 0 \qquad -d \leq x \leq d \qquad 0 < y < c$$

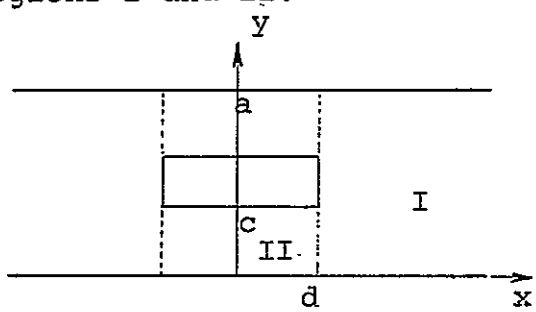

Fig. 1 Cross-section of waveguide

The two outer conductors are at zero potential and the inner conductor has normalized potential of unity.

Laplace's equation is solved in region I by separation of variables under application of the boundary conditions:

$$\phi_1 = 0 \quad @ \; y = 0 \;\text{ and }\; y = a \qquad ; \qquad \phi_1 \to 0 \quad \text{as} \quad x \to \infty$$

The solution may be written as the series

$$\phi_1(x,y) = \sum_{n=1,3,\cdots} A_n e^{-\frac{n\pi}{a}(x-d)} \sin \frac{n\pi}{a} y \qquad x \geq d \;;\; 0 \leq y \leq \frac{a}{2}$$

In region II, the solution to the potential is constructed by the following consideration: If the inner conductor is extended to infinity in both +x and -x directions, the potential in region II approaches the linear variation shown in figure 2.

$$\phi_2' = y/c \qquad 0 \leq y \leq c$$

$$\phi_2' = 1 \qquad c \leq y \leq a/2$$

This can be represented in a series of the form

$$\phi_2' = \sum_{n=1,3,\cdots} B_n \sin \frac{n\pi}{a} y$$

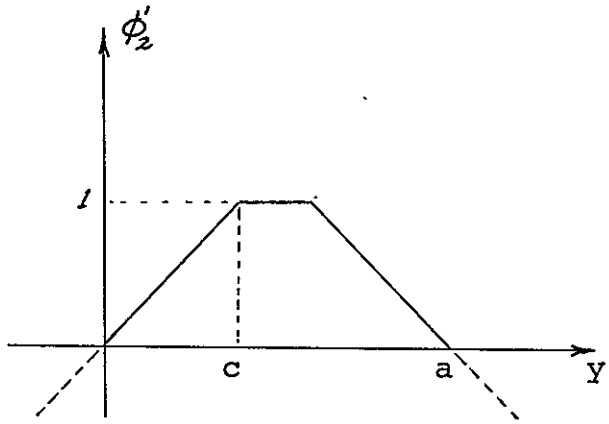

Fig. 2 Potential distribution for infinite-width slab

in which the B's are the Fourier coefficients and may readily be calculated. In the case of a slab of finite width, the potential distribution in region II will deviate from the above linear form by a function $\Delta\phi_2$. $\Delta\phi_2$ is written as superposition of two contributions, $\Delta_1\phi_2$ and $\Delta_2\phi_2$

$$\Delta\phi_2 = \Delta_1\phi_2 + \Delta_2\phi_2$$

$\Delta_1\phi_2$ is the deviation from the linear distribution as a result of removing the part of the slab where $x \leq -d$ (Fig. 3-a); $\Delta_2\phi_2$ is the deviation due to the removal of the part of the slab where $x \geq d$ (Fig. 3-b).

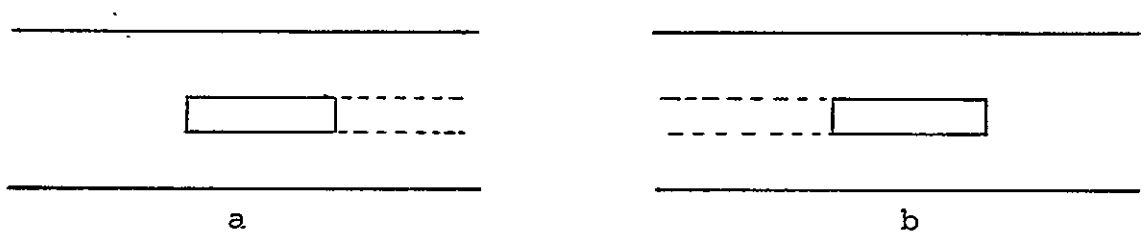

Fig. 3 Cross section of guide with semi-infinite slab

$\Delta_1\phi_2$ may be expressed by a Fourier series

$$\Delta_1\phi_2 = \sum_{m=1,2,\cdots} C_m' \, e^{-\frac{m\pi}{c}(x+d)} \sin\frac{m\pi}{c}y \qquad 0\le y\le c \;,\; x>-d$$

Similarly, $\Delta_2\phi_2$ is expressed as

$$\Delta_2\phi_2 = \sum_{m=1,2,\cdots} C_m' \, e^{\frac{m\pi}{c}(x-d)} \sin\frac{m\pi}{c}y \qquad 0\le y\le c \qquad x<d$$

Note that $\Delta_1\phi_2$ and $\Delta_2\phi_2$ are equal to zero when x approaches $+\infty$ and $-\infty$ respectively. Also, it is evident that by symmetry, the constants of the two series are identically C_m'. The total deviation is found to be

$$\Delta\phi_2 = \Delta_1\phi_2 + \Delta_2\phi_2$$

$$= \sum_{m=1,2,\cdots} C_m' \, e^{-\frac{m\pi}{c}d}\left(e^{-\frac{m\pi}{c}x} + e^{\frac{m\pi}{c}x}\right)\sin\frac{m\pi}{c}y \qquad \begin{matrix} 0\le y\le c \\ -d\le x\le d \end{matrix}$$

$$= \sum_{m=1,2,\cdots} C_m \cosh\frac{m\pi}{c}x \sin\frac{m\pi}{c}y$$

where

$$C_m = 2\,C_m' \, e^{-\frac{m\pi}{c}d} \,.$$

The total field in region II is $\phi_2 = \phi_2' + \Delta\phi_2$ which may be written in either of the following two forms:

$$\phi_2 = \begin{cases} \displaystyle\sum_{n=1,3,\cdots} B_n \sin\frac{n\pi}{a}y + \sum_{m=1,2,\cdots} C_m \cosh\frac{m\pi}{c}x \sin\frac{m\pi}{c}y & 0\le y\le c \\ \text{or} & \\ \frac{1}{c}y \quad + \quad " & \\ \displaystyle\sum_{n=1,3,\cdots} B_n \sin\frac{n\pi}{a}y & c\le y\le \frac{a}{2} \\ \text{or} & \\ 1 & \end{cases}$$

Final Equations for Potential

Rewriting the relations for the potential in each region we have:

In region (1), $x \geq d$

$$\phi_1(x,y) = \sum_{n=1,3,\cdots} A_n e^{-\frac{n\pi}{a}(x-d)} \sin \frac{n\pi}{a} y \qquad 0 \leq y \leq \frac{a}{2} \tag{1}$$

In region (2), $d \geq x \geq -d$, the field may be written in two forms

$$\phi_2(x,y) = \sum_{n=1,3,\cdots} B_n \sin \frac{n\pi}{a} y + \sum_{m=1,2,\cdots} C_m \cosh \frac{m\pi}{c} x \sin \frac{m\pi}{c} y \qquad 0 \leq y < c$$

$$\phi_2(x,y) = \sum_{n=1,3,\cdots} B_n \sin \frac{n\pi}{a} y \qquad c \leq y \leq a/2 \tag{2}$$

or

$$\phi_2(x,y) = \frac{1}{c} y + \sum_{m=1,2,\cdots} C_m \cosh \frac{m\pi}{c} x \sin \frac{m\pi}{c} y \qquad 0 \leq y < c$$

$$\phi_2(x,y) = 1 \qquad c \leq y \leq a/2 \tag{3}$$

Field Matching

The coefficients A_n and C_m are to be evaluated. This is done by matching the potential and the electric field at the boundary between the two regions, obtaining two systems of equations involving A's and C's and solving them simultaneously.

Matching ϕ:

Evaluating and equating equations (1) and (2) or (1) and (3) at $x = d$ we obtain

$$\sum_{n=1,3,\cdots} A_n \sin \frac{n\pi}{a} y = \sum_{n=1,3,\cdots} B_n \sin \frac{n\pi}{a} y + \sum_{m=1,2,\cdots} C_m \cosh \frac{m\pi d}{c} \sin \frac{m\pi}{c} y$$

$$\sum_{n=1,3,\cdots} A_n \sin \frac{n\pi}{a} y = \sum_{n=1,3,\cdots} B_n \sin \frac{n\pi}{a} y \tag{4}$$

or

$$\sum_{n=1,3,\cdots} A_n \sin\frac{n\pi}{a}y = \frac{1}{c}y + \sum_{m=1,2,\cdots} C_m \cosh\frac{m\pi d}{c}\sin\frac{m\pi}{c}y \qquad 0\le y<c$$

$$\sum_{n=1,3,\cdots} A_n \sin\frac{n\pi}{a}y = 1 \qquad c\le y\le a/2 \tag{5}$$

Each equation in (4) or (5) is multiplied by $\sin\frac{n'\pi}{a}y$ and integrated in its proper region.

Equation (4) gives:

$$\int_0^c \sum_{n=1,3,\cdots}(A_n - B_n)\sin\frac{n\pi}{a}y\sin\frac{n'\pi}{a}y\,dy = \int_0^c \sum_{m=1,2,\cdots} C_m \cosh\frac{m\pi d}{c}\sin\frac{m\pi}{c}y\sin\frac{n'\pi}{a}y\,dy$$

$$\int_c^{a/2} \sum_{n=1,3,\cdots}(A_n - B_n)\sin\frac{n\pi}{a}y\sin\frac{n'\pi}{a}y\,dy = 0$$

Adding the above and noting the orthogonality property of the left-hand side, we have:

$$\frac{1}{4}a\,(A_n - B_n) = \sum_{m=1,2,\cdots} C_m F_{mn} \tag{6}$$

where

$$F_{mn} = \cosh\frac{m\pi}{c}d\int_0^c \sin\frac{m\pi}{c}y\sin\frac{n\pi}{a}y\,dy$$

Equation (5) gives

$$\int_0^c \sum_{n=1,3,\cdots} A_n \sin\frac{n\pi}{a}y\sin\frac{n'\pi}{a}y\,dy = \frac{1}{c}\int_0^c y\sin\frac{n'\pi}{a}y\,dy +$$

$$\int_0^c \sum_{m=1,2,\cdots} C_m \cosh\frac{m\pi}{c}d\sin\frac{m\pi}{c}y\sin\frac{n'\pi}{a}y\,dy$$

$$\int_c^{a/2} \sum_{n=1,3,\cdots} A_n \sin\frac{n\pi}{a}y\sin\frac{n'\pi}{a}y\,dy = \int_c^{a/2} \sin\frac{n'\pi}{a}y\,dy$$

Again adding the two equations and using the orthogonality on left-hand side yields

$$\frac{1}{4} a A_n = \frac{a^2}{(n\pi)^2 c} \sin\frac{n\pi c}{a} + \sum_{m=1,2,\cdots} C_m F_{mn} \tag{7}$$

which is equivalent to Eq. (6). We observe that the first right-hand term corresponds to B_n for the trapezoidal distribution according to Fig. 2. Equations (6) or (7) actually give only one system for a relationship between the A's and C's. To find a second system of equations, another field quantity has to be matched at x = d. There are two possibilities: (a) matching E_x at x = d, (b) matching E_y at x = d.

Matching E_x:

In each region

$$E_x = \frac{\partial \phi}{\partial x}$$

In region (I),

$$E_x = \sum_{n=1,3,\cdots} \left(\frac{-n\pi}{a}\right) A_n e^{-\frac{n\pi}{a}(x-d)} \sin\frac{n\pi}{a} y \qquad 0 \le y \le a/2$$

In region (II)

$$E_x = \sum_{m=1,2,\cdots} \frac{m\pi}{c} C_m \sinh\frac{m\pi}{c} x \sin\frac{m\pi}{c} y \qquad 0 \le y < c$$

Evaluating and equating the two equations at x = d gives

$$\sum_{n=1,3,\cdots} \left(\frac{-n\pi}{a}\right) A_n \sin\frac{n\pi}{a} y = \sum_{m=1,2,\cdots} \frac{m\pi}{c} C_m \sinh\frac{m\pi d}{c} \sin\frac{m\pi}{c} y. \qquad 0 \le y < c$$

Multiplying both sides by $\sin\frac{m'\pi}{c} y$ and integrating from 0 to c and noting orthogonality property of the right-hand side, we

obtain

$$\sum_{n=1,3,\cdots} A_n G_{nm} = \frac{m\pi}{2} \sinh \frac{m\pi}{c} d \cdot C_m \qquad (8)$$

where

$$G_{nm} = -\frac{n\pi}{a} \int_0^c \sin \frac{n\pi}{a} y \sin \frac{n\pi}{c} y \, dy$$

Matching E_y:

In each region E_y is found by:

$$E_y = \frac{\partial \phi}{\partial y}$$

In region (I)

$$E_y = \sum_{n=1,3,\cdots} \frac{n\pi}{a} A_n e^{-\frac{n\pi}{a}(x-d)} \cos \frac{n\pi}{a} y \qquad 0 \le y \le a/2$$

In region (II)

$$\begin{cases} E_y = \frac{1}{c} + \sum_{m=1,2,\cdots} \frac{m\pi}{c} C_m \cosh \frac{m\pi}{c} x \cos \frac{m\pi}{c} y & 0 \le y \le c \\ E_y = 0 & c < y \le a/2 \end{cases}$$

Note that the result of obtaining the E_y from (2) or (3) should be equivalent. That is, the above set of equations giving E_y in region II is equivalent to the relation obtained from (2):

$$E_y = \sum_{n=1,3,\cdots} \frac{n\pi}{a} B_n \cos \frac{n\pi}{a} y + \sum \frac{m\pi}{c} C_m \cosh \frac{m\pi}{c} x \cos \frac{m\pi}{c} y \qquad 0 \le y \le c$$

$$E_y = \sum_{n=1,3,\cdots} \frac{n\pi}{a} B_n \cos \frac{n\pi y}{a} \qquad c < y \le a/2$$

Hence in matching E_y at $x = d$, either of the above representations may be used. For completeness, let us use both and find the resultant relations.

Evaluate E_y at $x = d$ from both relations and equate the result.

$$\begin{cases} \sum_{n=1,3,\cdots} \frac{n\pi}{a} A_n \cos\frac{n\pi}{a} y = \sum_{n=1,3,\cdots} \frac{n\pi}{a} B_n \cos\frac{n\pi}{a} y + \sum_{m=1,2,\cdots} \frac{m\pi}{c} \cosh\frac{m\pi}{c} d \cos\frac{m\pi}{c} y & 0 \le y \le c \\ \sum_{n=1,3,\cdots} \frac{n\pi}{a} A_n \cos\frac{n\pi}{a} y = \sum_{n=1,3,\cdots} \frac{n\pi}{a} B_n \cos\frac{n\pi}{a} y & c < y \le a/2 \end{cases} \tag{9}$$

or

$$\begin{cases} \sum_{n=1,3,\cdots} \frac{n\pi}{a} A_n \cos\frac{n\pi}{a} y = \frac{1}{c} + \sum_{m=1,2,\cdots} C_m \frac{m\pi}{c} \cosh\frac{m\pi}{c} d \cos\frac{m\pi}{c} y & 0 \le y \le c \\ \sum_{n=1,3,\cdots} \frac{n\pi}{a} A_n \cos\frac{n\pi}{a} y = 0 & c < y \le a/2 \end{cases} \tag{10}$$

Each equation in (9) is multiplied by $\cos\frac{n'\pi}{a} y$ and integrated in its proper region.

$$\int_0^c \sum_n \frac{n\pi}{a} A_n \cos\frac{n\pi}{a} y \cos\frac{n'\pi}{a} y \, dy = \int_0^c \sum_n \frac{n\pi}{a} B_n \cos\frac{n\pi}{a} y \cos\frac{n'\pi}{a} y \, dy + \int_0^c \sum_m \frac{m\pi}{c} C_m \cosh\frac{m\pi d}{c} \cos\frac{n'\pi}{a} y \cos\frac{m\pi}{c} y \, dy$$

$$\int_c^{a/2} \sum_n \frac{n\pi}{a} A_n \cos\frac{n\pi}{a} y \cos\frac{n'\pi}{a} y \, dy = \int_c^{a/2} \sum_n \frac{n\pi}{a} B_n \cos\frac{n\pi}{a} y \cos\frac{n'\pi}{a} y \, dy + 0 .$$

Add the two equations, use orthogonal properties in (0 - a) region to obtain

$$\frac{1}{4} a \frac{n\pi}{a} (A_n - B_n) = \sum_{m=1,2,\cdots} C_m F'_{mn} \tag{11}$$

where

$$F'_{mn} = \frac{m\pi}{c} \cosh\frac{m\pi d}{c} \int_0^c \cos\frac{m\pi}{c} y \cos\frac{n\pi}{a} y \, dy$$

If Eq. (10) is multiplied by $\cos \frac{n'\pi}{a} y$, integrated in proper region and each part of it added, we obtain

$$\frac{1}{4} a \frac{n\pi}{a} A_n = \int_0^c \frac{1}{c} \cos \frac{n\pi}{a} y \, dy + \sum_{m=1,2,\cdots} C_m F'_{mn} \tag{12}$$

Summary of the result of field matching is as follows:

Matching ϕ at x = d:

$$\frac{1}{4} a (A_n - B_n) = \sum_{m=1,2,\cdots} C_m F_{mn} \tag{6}$$

or

$$\frac{1}{4} a A_n - \frac{a^2}{(n\pi)^2 c} \sin \frac{n\pi}{a} c = \sum_{m=1,2,\cdots} C_m F_{mn} \tag{7}$$

Matching E_x at x = d:

$$\sum_{n=1,3,\cdots} A_n \cdot G_{nm} = \frac{m\pi}{2} \sinh \frac{m\pi d}{c} \cdot C_m \tag{8}$$

Matching E_y at x = d:

$$\frac{1}{4} n\pi (A_n - B_n) = \sum_{m=1,2,\cdots} C_m \cdot F'_{mn} \tag{11}$$

or

$$\frac{1}{4} n\pi A_n - \frac{1}{c} \int_0^c \cos \frac{n\pi}{a} y \, dy = \sum_{m=1,2,\cdots} C_m \cdot F'_{mn} \tag{12}$$

To find A's and C's from the above equation systems, two of the equations (6), (7), (8), (11), and (12) must be solved simultaneously. Obviously Eqs. (6) and (7) taken simultaneously will not give any useful result. Similarly (11) and (12) are not independent.

The other possible combinations which should be investigated are:

Eqs. (6) or (7) solved with Eq. (8),

Eqs. (6) or (7) solved with Eqs. (11) or (12),

Eqs. (11) or (12) solved with Eq. (8).

Solving [(6) or (7)] with [(11) or (12)]:

$$A_n - B_n = \frac{4}{a} \sum_m C_m F_{mn}$$

$$A_n - B_n = \frac{4}{n\pi} \sum_m C_m F'_{mn}$$

$$\sum_m C_m \left(\frac{1}{a} F_{mn} - \frac{1}{n\pi} F'_{mn} \right) = 0$$

$$F_{mn} = \cosh \frac{m\pi d}{c} \cdot \frac{(-1)^{m+1}}{\pi} \cdot \sin \frac{n\pi c}{a} \left[\frac{m/c}{(m/c)^2 - (n/a)^2} \right] = K \cdot \frac{m}{c}$$

$$F'_{mn} = \frac{m\pi}{c} \cdot \cosh \frac{m\pi d}{c} \cdot \frac{(-1)^{m+1}}{\pi} \sin \frac{n\pi c}{a} \left[\frac{n/a}{(m/c)^2 - (n/a)^2} \right] = K \cdot \frac{mn\pi}{ac}$$

$$\sum_m C_m \left(\frac{1}{a} K \cdot \frac{m}{a} - \frac{1}{n\pi} K \cdot \frac{mn\pi}{ac} \right) \equiv 0$$

Therefore, no useful information is obtained.

Solving [(6) or (7)] with [(8)]:

Find C_m from (8) and substitute in (7)

$$C_m = \frac{2}{m\pi} \frac{1}{\sinh \frac{m\pi d}{c}} \sum_{n=1,3\ldots} A_n \cdot G_{nm}$$

$$\frac{1}{4} a A_k - \frac{a^2}{(k\pi)^2 c} \sin \frac{k\pi c}{a} = \sum_{m=1,2,\ldots} \frac{2}{m\pi} \frac{1}{\sinh \frac{m\pi d}{c}} \sum A_n \cdot G_{nm} \cdot F_{mk}$$

$$A_k - \frac{8}{\pi a} \sum_{n=1,3,\ldots} A_n \cdot \sum_{m=1,2,\ldots} \frac{G_{nm} \cdot F_{mk}}{\sinh \frac{m\pi d}{c}} = \frac{4a \sin \frac{k\pi c}{a}}{(k\pi)^2 c} \qquad (13)$$

$$k = 1, 3, 5, \ldots$$

This is solved by taking a finite number of terms, then A's are substituted in (8) to find C's.

Solving [(8)] with [(11) or (12)]:

Again C_m from Eq. (8) is substituted in Eq. (11):

$$\frac{1}{4}k\pi(A_k - B_k) = \sum_{m=1,2,\cdots} \frac{2}{m\pi} \frac{1}{\sinh \frac{m\pi d}{c}} \cdot \sum_{n=1,3,\cdots} A_n \cdot G_{nm} \cdot F'_{mk}$$

or

$$\sum_{n=1,3,\cdots} A_n \sum_{m=1,2,\cdots} \frac{2}{m\pi \sinh \frac{m\pi d}{c}} \cdot G_{nm} F'_{mk} - \frac{1}{4}k\pi A_k = -\frac{1}{4}k\pi B_k \qquad (14)$$

$$k = 1,3,5,\cdots$$

Again, the above may be expanded by choosing a finite number of terms and the resulting system of equations is solved for A's. The A's are substituted in either Eq. (8) or Eq. (11) to find C's.

Computation of Capacitance and Impedance

Solutions of Eq. (13) were obtained for the cases where each series was approximated by its first 20, 25, 30, 35 and 40 terms. It was observed that the value of the capacitance fluctuated only in the 4th significant figure (less than 0.1%). The results computed here are obtained from the 20-term approximation of Eq. (13) in which case indices k, n, and m are given the values 1,3,5 . . ., 39; 1, 3, 5 . . . 39; and 1, 2, 3, . . . 20 respectively.

Once the coefficients A's and C's are computed, the field

components may be determined by differentiating the potential functions. The total charge per unit length of the guide is obtained by integrating the normal component of the electric density vector at the surface of the guide walls. The capacitance is by definition the ratio of total charge to the potential difference. Considering the symmetry of the structure, we write:

$$C = \frac{Q}{V} = \frac{1}{V}\, 4\epsilon_0 \left\{ \int_0^d \left[E_y^{II} \right]_{y=0} dx + \int_d^\infty \left[E_y^{I} \right]_{y=0} dx \right\}$$

Evaluating the integrals and substituting $V = 1$, the capacitance is

$$C = 4\epsilon_0 \left\{ \frac{d}{c} + \sum_{m=1,2,\ldots} C_m \sinh \frac{m\pi d}{c} + \sum_{n=1,3,\ldots} A_n \right\}$$

The line impedance is

$$Z_0 = \frac{1}{C\, c_0}$$

where c_0 is the velocity of light.

Fig. 4 shows graph of line impedance versus c/a, with 2d/a as parameter.

Figures 5 and 6 show the comparison of the potential in the guide computed from the field-matching method and the numerical technique described in the appendix for one particular case where c/a=1.1/4, 2d/a = 1/2. It is observed that the two results agree quite well. The maximum deviations occur along the lines originating from the corners of the inner conductor and in the vicinity of the corner.

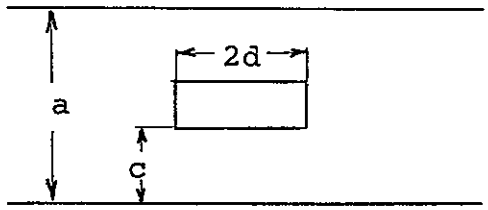

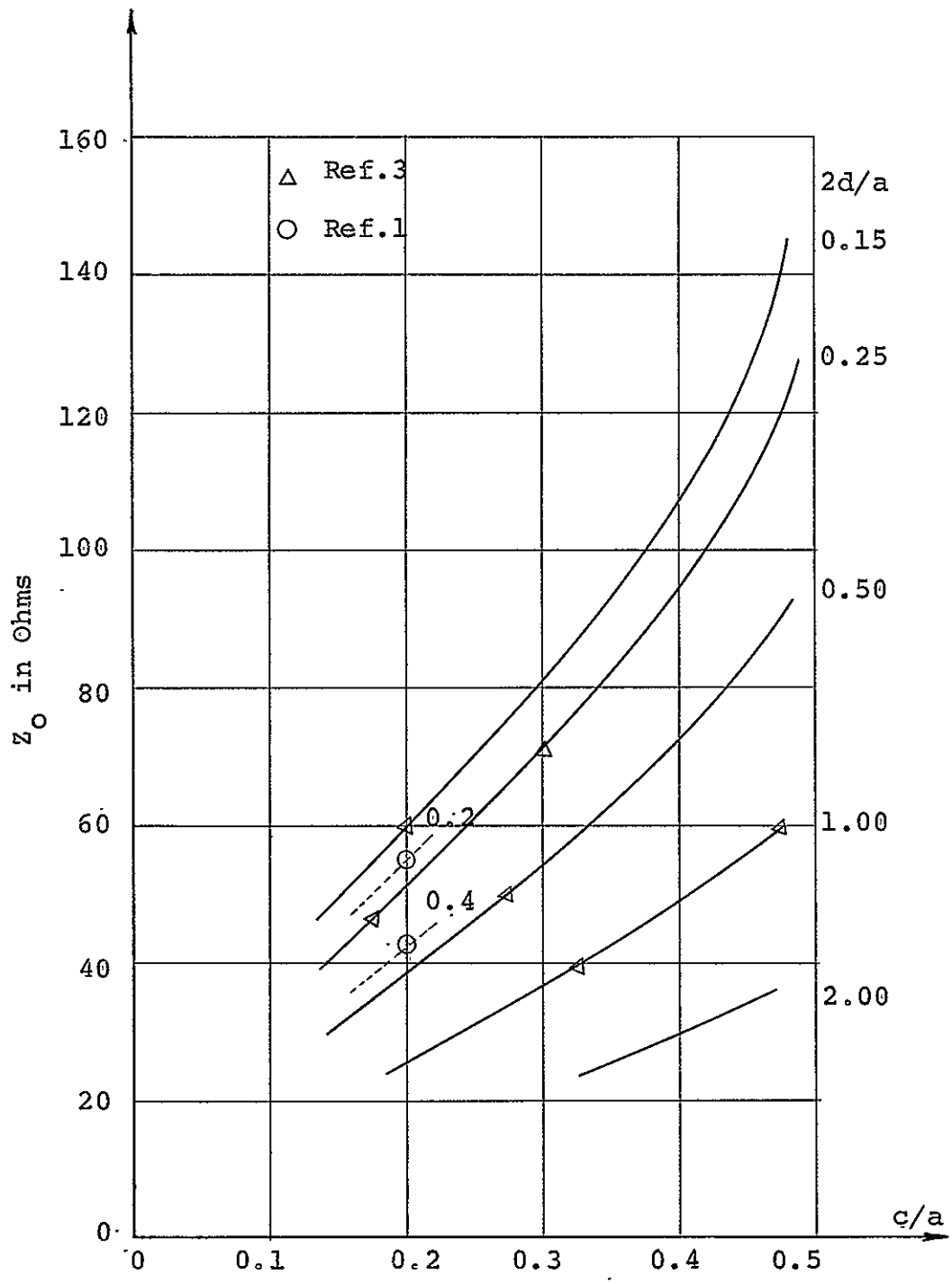

Fig. 4 Characteristic impedance vs c/a with 2d/a as parameter.

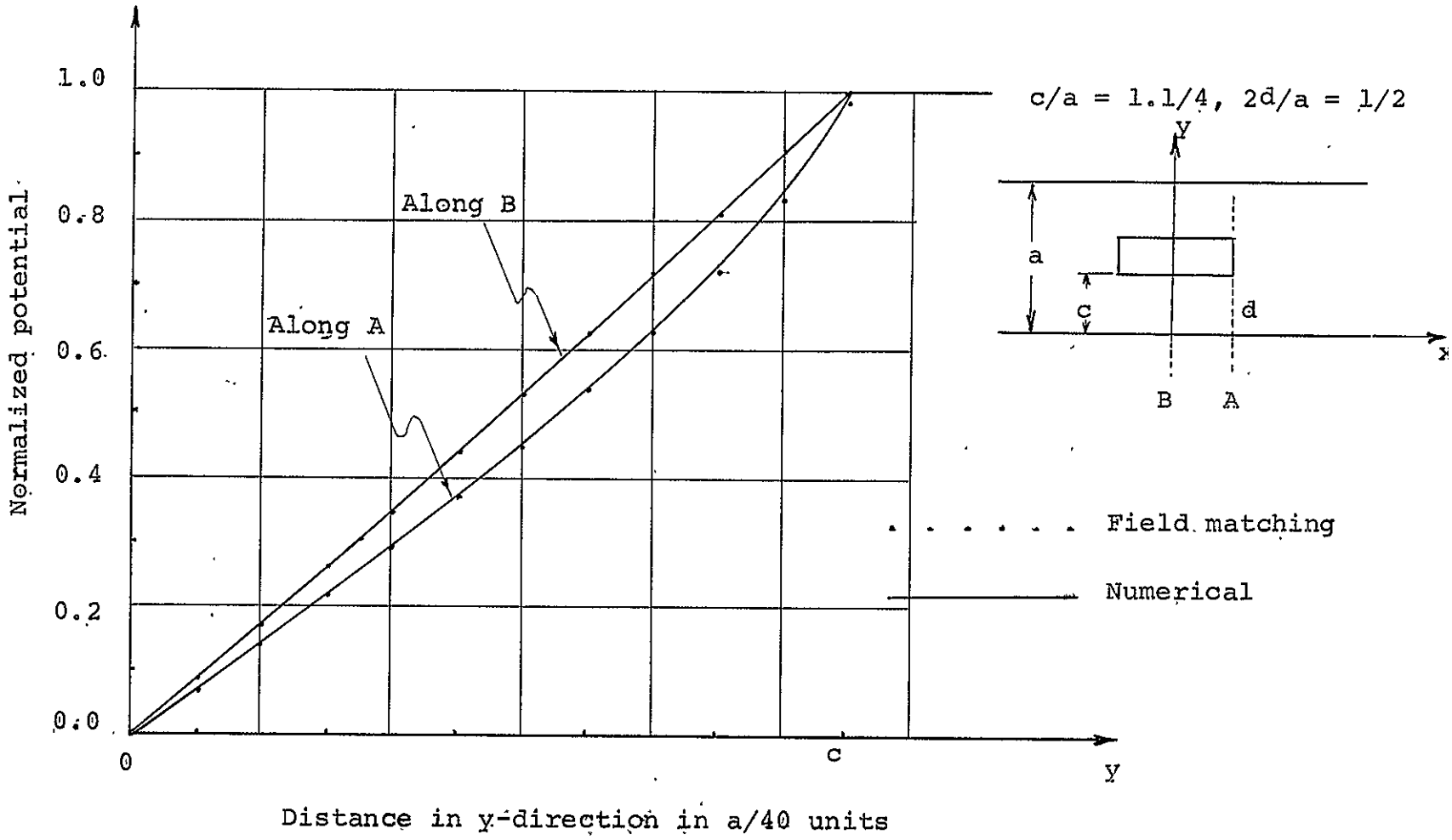

Fig. 5 Potential variations in y-direction, (the dots indicate the result of field-matching method).

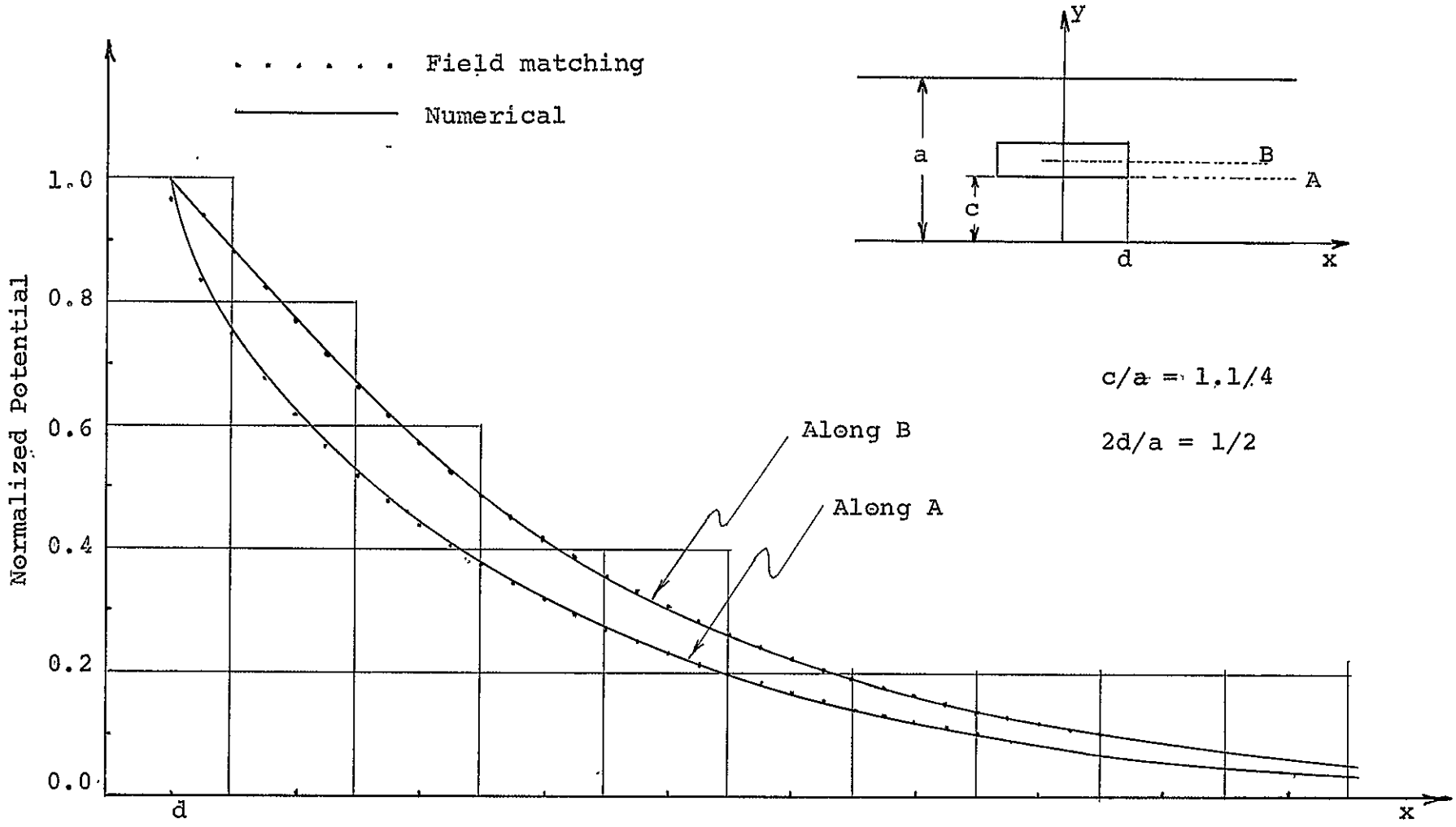

Distance in x-direction in a/40 units

Fig. 6 Potential variations in x-direction. (the dots indicate the result of field-matching method).

APPENDIX

A numerical solution of the potential in the waveguide is compared with potential obtained from the field matching method. The numerical technique outlined here is based on finite-difference solution of Laplace's equation.[2]

The potential near any point (x,y) may be expanded in a Taylor series disregarding higher-order terms

$$\phi(x+\Delta x,y) \cong \phi(x,y) + \Delta x \frac{\partial \phi}{\partial x} + \frac{\Delta x^2}{2} \frac{\partial^2 \phi}{\partial x^2}$$

$$\phi(x-\Delta x,y) \cong \phi(x,y) - \Delta x \frac{\partial \phi}{\partial x} + \frac{\Delta x^2}{2} \frac{\partial^2 \phi}{\partial x^2}$$

$$\phi(x, y+\Delta y) \cong \phi(x,y) + \Delta y \frac{\partial \phi}{\partial y} + \frac{\Delta y^2}{2} \frac{\partial^2 \phi}{\partial y^2}$$

$$\phi(x, y-\Delta y) \cong \phi(x,y) - \Delta y \frac{\partial \phi}{\partial y} + \frac{\Delta y^2}{2} \frac{\partial^2 \phi}{\partial y^2}$$

Combining the first two relations, we obtain

$$\frac{\partial^2 \phi}{\partial x^2} \cong \frac{\phi(x+\Delta x, y) - 2\phi(x,y) + \phi(x-\Delta x, y)}{\Delta x^2}$$

Combining the next two equations gives

$$\frac{\partial^2 \phi}{\partial y^2} \cong \frac{\phi(x, y+\Delta y) - 2\phi(x,y) + \phi(x, y-\Delta y)}{\Delta y^2}$$

If $\frac{\partial^2 \phi}{\partial x^2}$ and $\frac{\partial^2 \phi}{\partial y^2}$ are substituted in the Laplace equation and $\Delta x = \Delta y = h$, we obtain

$$\phi(x,y) \cong \frac{1}{4}\left[\phi(x+h,y) + \phi(x-h,y) + \phi(x,y+h) + \phi(x,y-h)\right]$$

In order to utilize this relation, the cross-section of the waveguide is divided into a grid where the size of each mesh is

h × h. According to the above equation, the potential at each node (grid intersection) is obtained by averaging the potentials of the four neighboring points (see Fig.(7). After the potentials of all the nodes which do not lie on boundaries are successively computed, the process is repeated over again; each time using the previous values until each node-potential converges to a fixed value or until its variations become smaller than a prescribed tolerance.

The convergence of the iterations may be improved by introducing a procedure used in relaxation method for difference equations. The procedure is to purposely under- or over-approximate the potential at each step. If the change of potential after the kth and (k + 1)th iteration is R^k

$$R^k = \phi^{k+1} - \phi^k$$

then, instead of finding ϕ^{k+1} from

$$\phi^{k+1} = \phi^k + R^k$$

we use

$$\phi^{k+1} = \phi^k + \beta R^k$$

where β may be less than or greater than unity and is dependent on the geometry.

As shown in Fig 7, the grid lines are chosen such that each boundary or known potential surface coincides with a grid line. It should be noted that the accuracy of the converged potential values is dependent on the fineness of the mesh.

In Fig. 7 the boundary conditions are given by the zero potential on the walls at y = 0 and y = a. In addition, it is

assumed that the potential is negligible at $\pm x_1$ for $x_1 \simeq 1.7$. This is justified since the potential variation in the x-direction is proportional to $\exp(-\frac{n\pi x}{a})$ and for $\frac{x}{a} \geq 1.5$ its magnitude drops to less than 0.01 of its value at the center conductor.

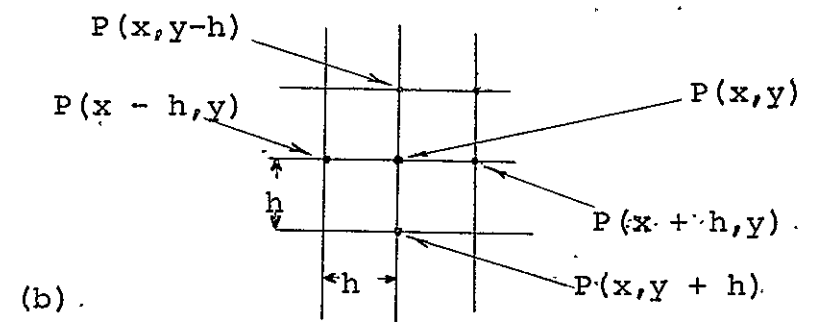

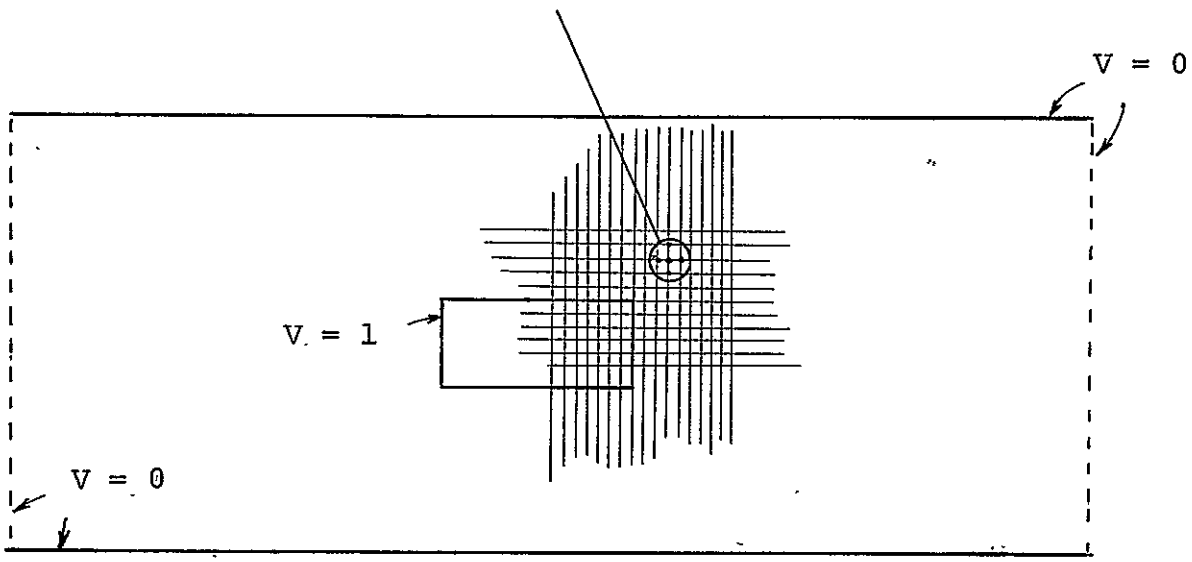

(a)

Fig. 7 (a) Cross-section of waveguide with grid

(b) Enlargement of the insert

Block Diagram of the Computer Program
for the Numerical Solution

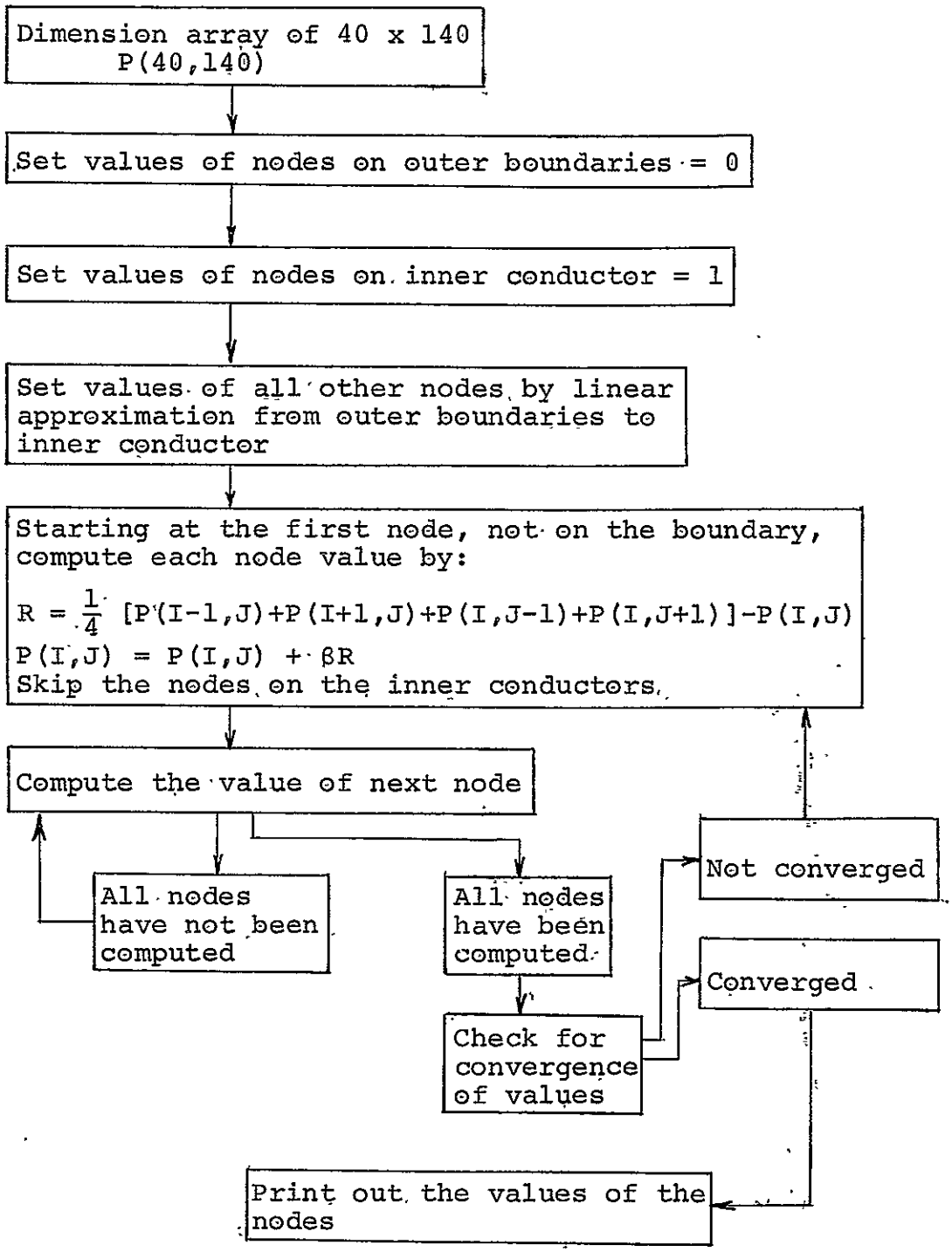

References

1. N. A. Begovich, "Capacity and Characteristic Impedance of Strip Transmission Lines with Rectangular Inner Conductors," IRE Trans. vol. MTT-3, pp. 127-136, March, 1953.

2. S. Ramo, J. R. Whinnery, and T. Van Duzer, Field & Waves in Communication Electronics, sec. 3.09 and 3.10, John Wiley & Sons, Inc., New York, 1965.

3. Private Communication from Dr. F. J. Tischer, EE Dept., N. C. State University.